UNIVERSITÀ DEGLI STUDI DI PADOVA

Dipartimento di Fisica e Astronomia "Galileo Galilei"

Master's Degree in Astrophysics and Cosmology

Final dissertation

Characterizing Light Scattering Sources in Gravitational-Wave Interferometers

Thesis supervisor
Prof. Giacomo Ciani

Candidate
Izumi Takimoto Schmiegelow

Thesis co-supervisors
Dr. Livia Conti
Dr. Giulio Favaro

Academic Year 2022/2023

Aos meus pais.

Abstract

Gravitational wave signals are currently detected with interferometers that measure extremely small deformations of space. This is done by monitoring changes in an interference pattern, that is also subject to various kinds of noise. Finding strategies to reduce these noises is thus essential to improve the sensitivity of gravitational wave detectors.

Stray light is one of the various causes of noise in current detectors and affects mostly the low-frequency end of the spectrum. It comprises any light beam that does not follow the intended path in the instrument, which can recombine with the main beam with a different phase and cause unwanted changes in the interference pattern. One of its causes is the scattering of light off optical and mechanical components in the detector, due to surface roughness or dust contaminants. The problem is intensified due to the strong seismic noise affecting these components, generating fluctuations in the phase of the scattered beam.

The work of this thesis consists of testing and upgrading an instrument that measures the amount of scattering caused by materials used in gravitational wave detectors. Measurement procedures were developed and contributions from background and systematic effects were estimated. Theoretical models that describe the scattering were reviewed and the Generalized Harvey-Shack model was tested on preliminary measurements made with the instrument.

Contents

1 Introduction

1.1 Gravitational Waves

Gravitational waves were predicted for the first time by Albert Einstein in 1916. According to his theory of general relativity, space and time are two sides of the same entity, *spacetime*. Spacetime can be thought of as a fabric that can be stretched and deformed by mass and energy. In this way, gravity is not described as a force, like in Newtonian physics, but as a curvature of spacetime. Free masses then move according to this curvature, following paths that minimize the spacetime interval, called *geodesics*. This is perceived as an acceleration by external observers.

When a mass moves in spacetime, this can create ripples in the fabric, which is what we call gravitational waves (GWs hereafter). As the wave propagates, it stretches spacetime in the plane perpendicular to its direction of propagation. When the GW passes through an object, the effect that we observe is a stretching of this object. For this reason, the amplitude of the GW is usually measured as "strain", which is the fractional change in length caused by the passing of the wave.

GW emission can be described with the "quadrupole formula" [14]. The quadrupole moment expresses the mass distribution of an object or system. The quadrupole formula states that GWs are emitted only if the second derivative of the quadrupole moment is different from zero, analogously to the emission of an electromagnetic wave from an electric dipole. Just like electromagnetic radiation is emitted from accelerated charges, GWs are emitted from accelerated masses.

Since spacetime is extremely stiff, GWs arriving on Earth from far away sources are generally minuscule in amplitude, and we can only hope to measure the ones produced by extremely large masses and accelerations. To have a reasonable detection rate, we need to consider extremely large masses moving at relativistic speeds to produce the wave. The easiest targets to detect are coalescing binary systems of very massive and compact objects, like black holes or neutron stars. Right before they merge, they rotate around the center of mass at extremely high speeds, generating strong gravitational waves. The fact that they emit strong signals is not the only factor making them easy to detect: unlike events like supernovae and other bursts, these systems can be easily modeled, so data analysis techniques have been developed to match the collected data to the expected signal, identifying them more easily. From the shape of the GW, it is possible to understand the characteristics of the emitting system and its evolution, which many times is invisible to us when observing only light emission.

Unlike electromagnetic radiation, GWs interact very weakly with matter, so they can travel long distances without being absorbed and distorted by the environment [9]. Therefore, GWs can carry essential information about extremely distant sources and the early universe that other methods do not allow us to obtain.

1.2 Gravitational Wave Detectors

The detection of gravitational waves was possible for the first time in 2015 by the LIGO-Virgo collaboration with the data of the second-generation interferometric detectors Advanced LIGO (aLIGO) in the US. Together with Advanced Virgo in Italy,

they use interferometry to measure the distortion of space due to the passing gravitational wave. They follow the principles of a Michelson interferometer but are more complex and very large to achieve greater sensitivities.

Current advanced detectors contain two arms built perpendicular to each other. In the case of aLIGO, they are 4 kilometers long, while those of AdVirgo are 3 kilometers long. At the point of intersection between the two arms, there is a beam splitter. A laser beam is sent toward it, where it is split into two beams of equal power that travel through each of the arms. At the end of the arms, the beams are reflected back by mirrors, which are used as test masses, and later recombined when they meet again at the beam splitter, interfering with each other.

The kind of interference of the two beams depends on the difference in path length through which they travel. This difference is tuned so as to give almost completely destructive interference at the output when no GWs are passing through the instrument, and it changes when a passing wave distorts the arms and displaces the test masses. The two arms are orthogonal matching the fact the GWs impact oppositely and maximally two orthogonal directions, changing the interference pattern. This way, we are able to measure the strain caused by the GW on the arms.

In practice, the positions of the mirrors are also affected by noise of various origins. Various strategies have been adopted to reduce these noises in current advanced detectors, and more methods will be implemented in future detectors for an even greater increase in sensitivity. The different sources of noise in AdVirgo and their intensities at each frequency are shown in Fig. 1.1, where the final sensitivity goal is also shown. The current sensitivity of the Virgo and LIGO detectors is shown in Fig. 1.2.

At lower frequencies (10 - 40 Hz) an important source of noise is *seismic noise*. It is caused by vibrations of the ground (that could be due to human activity or natural factors) that also cause the instrument to vibrate, thus moving the mirrors and generating phase oscillations in the laser beam. This noise is greatly reduced by using a suspension system for the test masses, which consists of multiple layers of pendulums attached to each other, reducing the noise at each pendulum. Due to this system, we are currently not limited by seismic noise in advanced detectors.

By the lowest pendulum of the mirror suspensions, another noise dominates over seismic noise, *thermal noise*, which dominates in the mid-frequency range (40 Hz - 300 Hz). Due to the temperature of the material, there is a small vibration of the mirror's surface. This vibration is linked to the mechanical dissipation in the mirror's material according to the fluctuation-dissipation theorem. Future detectors will have a cryogenic system, but in current detectors, this is reduced by using monolithic suspensions at the end of the pendulum cascade. A great effort is also being put into developing better mirror coatings to reduce mechanical losses.

One of the most important sources of noise is *quantum noise*, which affects the entire frequency range and dominates at high frequencies (300 Hz - 10 kHz). It is a consequence of the fact that the photon count rate in the laser beam follows Poissonian statistics, therefore creating fluctuations in the phase and amplitude of the light beam. The fluctuation in phase is called *shot noise* and it causes changes in the interference pattern, therefore disturbing the measurement of the GW signal. The fluctuation in amplitude is called *quantum radiation pressure noise* and it creates a movement of the end mirrors due to the varying force of the radiation striking the

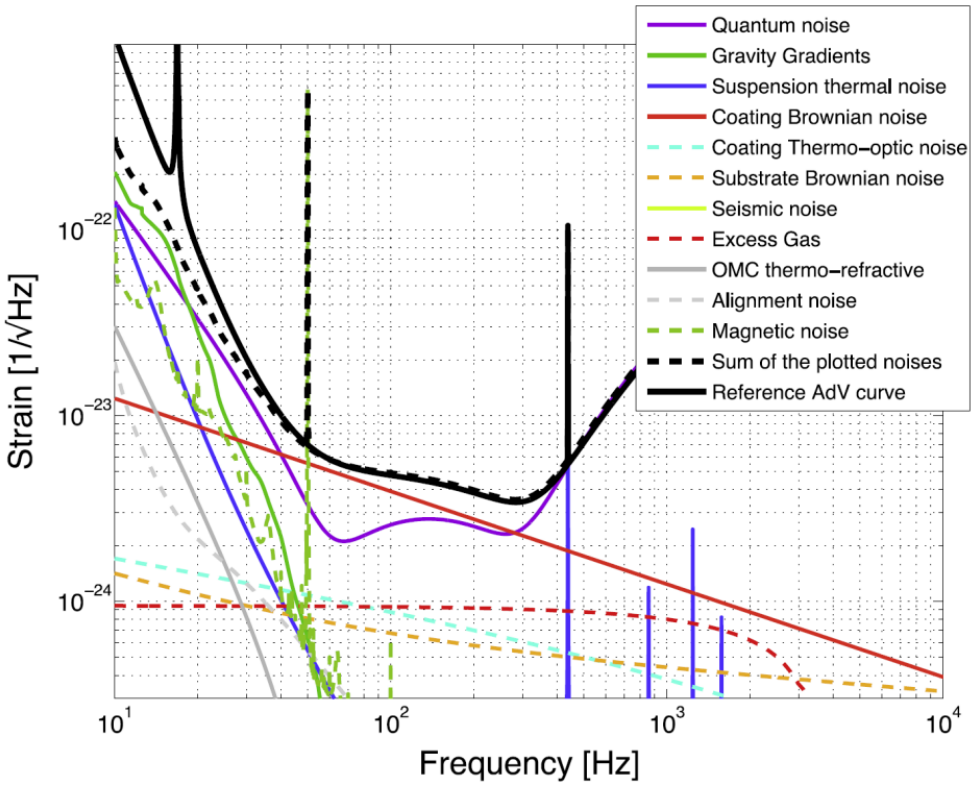

Figure 1.1: Final goal of AdVirgo sensitivity (solid black line), with individual contributions from different kinds of noise. The dashed black line shows the sum of all contributions. Image source: Acernese, F. et al (2018) [1].

surface. This movement translates into phase fluctuations of the reflected beam, also affecting the interference pattern. Quantum noise can be reduced by using *squeezing*, a form of quantum manipulation that allows us to decrease shot noise or radiation pressure noise at the expense of increasing the other one. This can be adjusted for specific frequencies, so we can choose the most appropriate compromise in each band.

Another source of noise that is present is *Newtonian noise*, dominating mostly at lower frequencies (< 5 Hz). It is caused by disturbances in the local gravitational field due to, for example, movements of air masses in the atmosphere, seismic activity in the soil, human activity, ocean waves, and basically anything that can affect the Earth's gravitational field. Since Newtonian noise affects the metric just like GWs, it is impossible for us to shield it. Nonetheless, we are currently not limited by it since other noises such as quantum noise and thermal noise are orders of magnitude higher at most frequencies in advanced detectors.

Together with shielding techniques and compensation systems, there are several ways to increase the sensitivity of the detector to ensure that it is high enough for the strain due to a GW to be bigger than the strain due to noise. One way to do this is by using Fabry-Perot cavities in the arms. At the beginning of each arm,

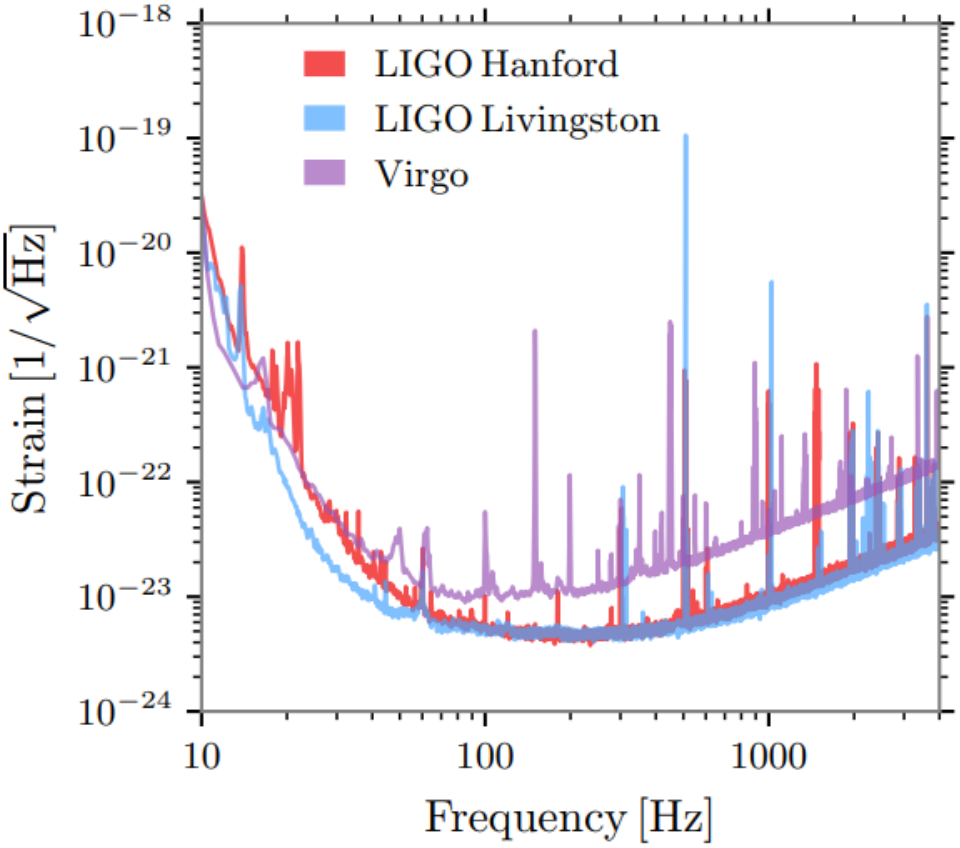

Figure 1.2: Sensitivity of advanced Virgo and LIGO detectors as of 2020. Image source: [28].

close to the beam splitter, an additional suspended mirror in the arm, trapping the photons between the two mirrors and making them bounce back and forth several times before returning to the beam splitter. This increases the length traveled by the photons, increasing the absolute change in path length due to the GW. The use of Fabry-Perot cavities has greatly increased the sensitivity of the detectors in the entire detection band, especially at lower frequencies. Fig. 1.3 illustrates this and other main optics used in the interferometer.

The signal-to-noise ratio is also increased by placing a *power recycling mirror* between the beam splitter and the laser output. When the laser light returning from the cavities reaches the beam splitter, part of the power is sent back to the laser output. This is maximal when the destructive interference condition is met on the output port. The power recycling mirror is placed between the laser output and the beam splitter, reflecting this power back to the arms. This creates resonance in the instrument, similar to considering the entire region between the end mirrors of the arms and the power recycling mirror as one cavity. This then increases the power inside the instrument, improving the sensitivity. Similarly, a *signal recycling mirror*

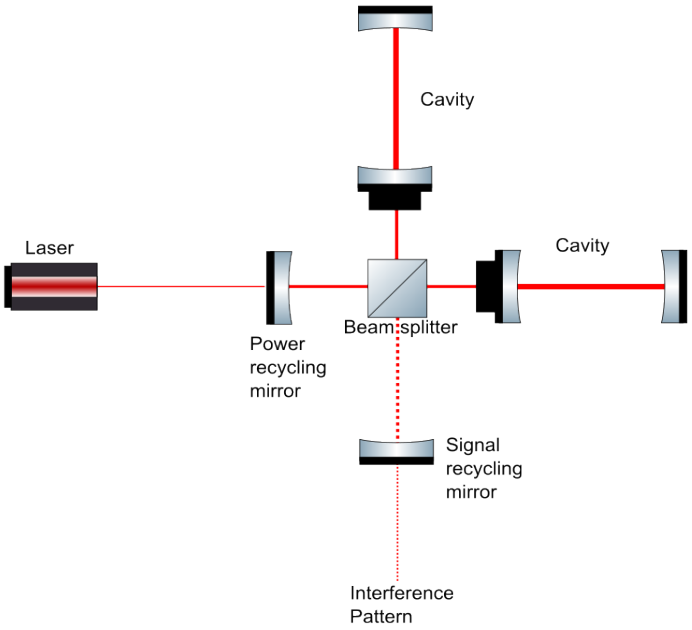

Figure 1.3: Optical scheme of an advanced detector. The most relevant elements are indicated, while others were omitted for simplification.

is placed between the beam splitter and the output port. This mirror is placed at a specific position such that it creates resonance at the frequency corresponding to the GW signal, enhancing the signal without amplifying the background noise.

With respect to the first generation of detectors, advanced detectors have improved in sensitivity by about an order of magnitude in a big frequency range [5]. The signal recycling mirror was one of the upgrades, and heavier mirrors were chosen to reduce thermal noise and to allow for the use of higher laser power, reducing the shot noise at higher frequencies without being compromised by radiation pressure noise. For this, a better thermal compensation system was also implemented. The mirrors were also improved with better materials, polishing, and coatings to reduce thermal noise, monolithic suspensions were used, and a squeezing system was implemented.

Among various other improvements, these upgrades have made the second generation of detectors sensitive enough to detect the first gravitational wave signals. However, the sources observed with these instruments are all mergers of binary systems involving black holes and/or neutron stars, and the current sensitivity of these detectors is estimated to allow for the detection of mergers at a maximum distance from Earth of about 130 Mpc [28]. The third generation of detectors is being designed with the aim of detecting more diverse signals coming from a larger distance.

The Einstein Telescope (ET) is an example of a third-generation detector. It will be built underground to avoid disturbances from vibrations on the surface. Instead of two perpendicular arms, it will have three arms in a triangular configuration, each of

them 10 kilometers long. There will be a total of 6 interferometers in the instrument, half of them optimized for high frequencies and half for low frequencies. The triangular configuration allows for a measurement of the polarization of the GW, which for now is only possible by combining detections by at least two different instruments. It is expected to reach sensitivities 10 times higher than second-generation detectors and to extend the freq of sensitivity, especially at the low-frequency bands, with respect to second-generation detectors. With such sensitivity, the ET will allow us to detect almost the entire population of binary black holes and neutron stars in the universe, enabling important studies of their origins, their nature, and cosmology [27].

1.3 The Issue of Stray Light

Although there are various methods to reduce most kinds of noise in the interferometer, the extra components added in the instrument for this can increase another source of noise, *stray light*. Stray light is any light in the instrument that does not follow the intended path. It has various causes, for example, when the light beam hits dust particles on optics or in the environment, when roughness and imperfections of the optical surfaces generate scattering, when diffraction happens from the surface's edges or when a fraction of it is reflected from imperfect anti-reflective coatings, generating ghost beams that can later be scattered on other components.

Stray light becomes a problem when it recombines with the main beam with a different phase. This effect is not easily modeled because the change in phase is dependent on the path length of the stray light beam, which in turn is subject to vibrations of the components that originate the scatter and reflect it. These vibrations are due to the fact that many components are not suspended like the test masses (or not suspended with the same performance), making them subject to strong seismic noise. Since the motion of the test masses is measured from a phase change of the light beam, the contribution from the stray light components reduces the sensitivity of the interferometer.

The recombination of stray light with the main beam can be described as an additional modulation of the electromagnetic field. It affects both the phase and amplitude of light. The modulation in the phase immediately translates into a change in the interference pattern, creating noise in the final signal. The modulation in the amplitude can create power fluctuations in the cavities, resulting in a displacement of the test masses through radiation pressure, which also creates a fluctuation in phase and affects the interference pattern.

Simulations of scattering elements affected by seismic noise at the LIGO Livingston interferometer have shown that stray light will most likely affect the sensitivity of the instrument at low frequencies (up to tens of Hz) when microseismic activity (small seismic disturbances, usually due to human activity or ocean waves) is high. However, the amplitude of stray light noise is still something that needs to be carefully studied for each individual detector, taking into account the materials used in the instrument, the locations at which scattering happens (which all have a different coupling to the final sensitivity), the recoupling mechanisms and the use of shielding measures, such as baffles, to prevent stray light from recombining with the main beam.

The aim of the thesis is to develop both experimental and modeling tools to improve our understanding of how light is scattered by various surfaces or materials.

In this context, I helped develop and build an upgraded version of a scatterometer, an instrument that measures the intensity and distribution of scattering from a sample. Additionally, I made some preliminary measurements and refined models to interpret the data. This can later be used to characterize different surfaces representative of the components used in the AdVirgo detector or that could be used in future detectors like the ET. Once the information on the scattering behavior of such surfaces is known, it can be used to select the best materials for the components of the interferometer considering the potential for stray light generation. It can also serve as a starting point for realistic simulations of stray light in the detector so that this issue can be better understood and addressed.

Section 2 presents basic concepts about radiometry and scattering of light and a review of surface scattering models. Section 3 describes the instrument in its previous version and in the new setup, including the work done as part of this thesis to study and improve the new design. Section 4 presents some preliminary measurements made to test the instrument and the chosen model, and the conclusion can be found in Section 5.

2 Scattering of Light

When a light beam crosses the boundary between two media, a fraction of it is reflected back to the first medium, and a fraction is transmitted through the second medium. If the surface boundary between the two media is perfectly smooth, we can describe the intensity of the reflection of light as a function of the angle from the surface's normal as a delta function centered in the specular direction. Similarly, the refracted component of light also has a well-defined direction. In this case, under the assumption of a plane wave, the light's path can be described by Fresnel's equations and Snell's law. However, when we have roughness in the surface, not all the light emerging from the interaction with the interface is in the directions predicted by these laws. This is what we call *surface scattering*.

If the second medium is homogeneous, reflection only occurs at the surface boundary between the two media. If it instead is heterogeneous, part of the light will be reflected and refracted inside the second medium by the regions of different material. This is called *volume scattering* [31]. Usually, both kinds of scattering are present. A volume filled with air particles is an example of a heterogeneous medium, where the gas molecules cause scattering. Moving into larger scales, dust particles in the air also generate scattering. In the same way, these particles can lay on surfaces, so their contribution to the scattering is added to the contribution by surface roughness. Moreover, other surface imperfections such as scratches have their own contribution to the total scattering. Typically, scattering due to surface roughness decreases with the wavelength of the incident light, while scattering due to particulates is less wavelength dependent.

2.1 Quantifying the Scatter

2.1.1 Radiometry

Before defining the quantities to describe scattered light, it is important to define some main radiometric quantities. Those are presented below.

- **Solid Angle**

  The solid angle defines an area A at a certain distance R from a given viewing point. This is often used to describe the area of the receiver, like a detector, as seen from the emitting source. It can be written as

  $$\Omega = \frac{A}{R^2}. \tag{2.1}$$

  Its unit is the steradian, abbreviated as sr.

- **Flux**

  The flux or power is the measurement of the amount of energy transfer per unit of time. It is typically measured in units of Joule per second (Js^{-1}) or Watts (W). It can be expressed as

  $$d\Phi = \frac{dQ(t)}{dt}, \tag{2.2}$$

  where $Q(t)$ is the energy of the electromagnetic field and t the time.

- **Radiance**

  The radiance is the flux emitted by a surface in a certain direction. For an object at an angle θ from the normal of the emitting surface, the surface area of the emitter that it observes is the projected area $A\cos\theta$, where A is the true surface area of the emitter. The receiver's surface area can be expressed as a solid angle Ω. This is illustrated in Fig. 2.1. The radiance is the flux per unit projected area and unit solid angle. It is expressed as

  $$L = \frac{d^2\Phi}{dA\cos\theta d\Omega}, \tag{2.3}$$

  The units used to express radiance are typically Watt per steradian per meter squared ($Wsr^{-1}m^{-2}$).

  An emitter that has constant radiance at all directions θ is called a Lambertian emitter.

- **Irradiance**

  Irradiance is the amount of flux per unit area of the receiver. Unlike radiance, it is independent of direction. It can be written as

  $$E = \frac{d\Phi}{dA} \tag{2.4}$$

  and it is typically expressed in units of Watt per meter squared (Wm^{-2})

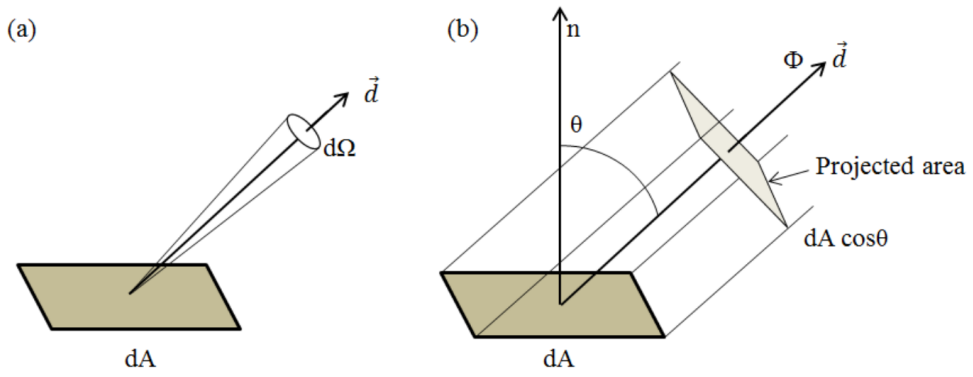

Figure 2.1: Geometry for the definition of radiance. (a) Differential solid angle of the receiver, (b) Projected area of the emitter as seen by the receiver. Image source: Won, Y. (2014) [32]

- **Intensity**

  The intensity is the differential flux $d\Phi$ emitted by the source per differential solid angle $d\Omega$ of the receiver.

$$I = \frac{d\Phi}{d\Omega} \tag{2.5}$$

2.1.2 BSDF and TIS

There are two main quantities that are useful to describe scattering: the *bidirectional scattering distribution function* (BSDF) and the *total integrated scattering* (TIS).

The BSDF was defined in 1970 by Nicodemus and is given by [23]:

$$BSDF(\theta_i, \phi_i, \theta_s, \phi_s) = \frac{dL(\theta_i, \phi_i, \theta_s, \phi_s)}{dE(\theta_i, \phi_i)}, \tag{2.6}$$

where dL is the differential radiance of the surface and dE is the differential irradiance incident on the surface. These values are functions of the angles θ_i and ϕ_i, which are the elevation and azimuth angles corresponding to the incident beam, and θ_s and ϕ_s, corresponding to the scattered beam. In essence, the BSDF describes the amount of scattering generated in a certain direction.

When referring to surface scattering, the BSDF can be divided into two contributions: the *bidirectional reflectance distribution function* (BRDF), which includes only the reflected part of the radiation, and the *bidirectional transmittance distribution function* (BTDF), which includes only the part of the radiation that was transmitted through the surface of the material. These definitions can be adapted to the case of volume scattering, defining them based on the scattering direction with respect to that of the incident light.

Despite its name, the TIS is typically defined as the integral of the BSDF over only half a sphere, covering either the reflected or the transmitted part of the scatter,

depending on which one is being studied:

$$TIS(\theta_i, \phi_i) = \int_0^{2\pi} \int_0^{\pi/2} BSDF(\theta_i, \phi_i, \theta_s, \phi_s) \cos(\theta_s) \sin(\theta_s) \, d\theta_s d\phi_s. \tag{2.7}$$

Here, the cosine term is included to account for the change in illuminated surface area of the sample viewed by an observer or detector at a certain angle θ_s from the surface's normal. The sine term is the Jacobian needed for integration in spherical coordinates.

The TIS represents the fraction of total incident power that is scattered by the surface in a certain hemisphere. It can also be written as

$$TIS = \frac{P_{scatt}}{P_{tot}}, \tag{2.8}$$

Where P_{scatt} is the scattered power in the hemisphere and P_{tot} is the total incident power. Due to energy conservation, the value of the TIS never exceeds 1.

2.2 Scattering due to Surface Roughness

2.2.1 Describing Surface Roughness

A rough surface exhibits deviations from its ideal height, denoted by $h(r)$, at different points r along a certain direction on the surface [12]. Fig. 2.2 illustrates a rough surface, with its mean height value indicated with a horizontal line, and a height deviation h. The root-mean-square (RMS) roughness σ_s is the root-mean-square of the height deviation at all points on this surface: $\sigma_s = \sqrt{< h(r)^2 >}$, if $< h(r) >= 0$. Very often for real surfaces, the height deviation distribution can be described as a Gaussian, in which case, σ_s is the standard deviation of the normal distribution [21].

The autocovariance (ACV) function describes how statistical height deviations at different points on the surface relate to each other. It can be written as [12] $C_s(r) = \sigma_s^2 < h(r + r')h(r') >$ for two points r and r'. A common ACV function for rough surfaces is well described by a Gaussian. Considering two perpendicular directions x and y on the surface, the Gaussian ACV function can be written as

$$C_s(x, y) = \sigma_s^2 e^{-r^2/l_c^2}, \tag{2.9}$$

with $r = \sqrt{x^2 + y^2}$, l_c the correlation length of the surface and σ_s the RMS roughness.

The surface power spectral density (PSD) is the Fourier transform of the ACV function. It gives the amount of height variation in the surface as a function of the spatial frequency. In the case of the Gaussian ACV from Eq. 2.9, the PSD is given by[21]:

$$PSD(f) = \pi l_c^2 \sigma_s^2 e^{-(\pi l_c f)^2}, \tag{2.10}$$

where f is the radial spatial frequency, given by $f = \sqrt{f_x^2 + f_y^2}$, with f_x and f_y the spatial frequencies in the x- and y-directions.

Experimental studies have shown that a Gaussian ACV function is most often not the case for polished surfaces fabricated with common techniques on glassy materials

[21]. These materials usually have an inverse power law behavior of the PSD, that can be described with the so-called "ABC function" or "K-Correlation function". This is given by [11]:

$$PSD(f_x)_{1D} = \frac{A}{[1 + (Bf_x)^2]^{C/2}}, \tag{2.11}$$

in 1 dimension, and

$$\begin{aligned} PSD(f)_{2D} &= K\frac{AB}{[1 + (Bf)^2]^{(C+1)/2}} \\ K &= \frac{1}{2\sqrt{\pi}}\frac{\Gamma((C+1)/2)}{\Gamma(C/2)}. \end{aligned} \tag{2.12}$$

in 2 dimensions, if we assume isotropic roughness. Here, Γ is the interpolation across real numbers of the factorial function for integers. Fig. 2.3 shows a plot of Eq. 2.13 in logarithmic scale. The parameter A indicates the value at low frequencies, B indicates the "knee" of the function, after which it decreases with a slope C. For simplification, we can collapse the K parameter from the two-dimensional expression into AB in the numerator, and the function can be written in the same form as the one-dimensional one:

$$PSD(f)_{2D} = \frac{A'}{[1 + (B'f)^2]^{C'/2}}, \tag{2.13}$$

However, the form in Eq. 2.12 can be useful if we want an analytical expression of the ACV function, which is then given by

$$C_s(r) = (2\pi)^{1/2}\frac{A}{B}\frac{2^{-C/2}}{\Gamma(C/2)}\left(\frac{2\pi r}{B}\right)^{(C-1)/2}\mathcal{K}_{(C-1)/2}\left(\frac{2\pi r}{B}\right), \tag{2.14}$$

where $\mathcal{K}_{(C-1)/2}$ is the modified Bessel function of the second kind.

The RMS roughness σ_s is given by the square root of the integral of the PSD over all spatial frequencies:

$$\sigma_s = \sqrt{\int_{-\infty}^{\infty}\int_{-\infty}^{\infty} PSD(f_x, f_y)df_x df_y}. \tag{2.15}$$

2.2.2 Scattering Models

Several models have been developed throughout history to describe surface scattering. This can be useful to fit scattering data from measurements, relate them to material and properties, and give an estimation of the TIS. The following subsections present an overview of existing models and elaborate on the Generalized Harvey-Shack model, which we use to fit our experimental data.

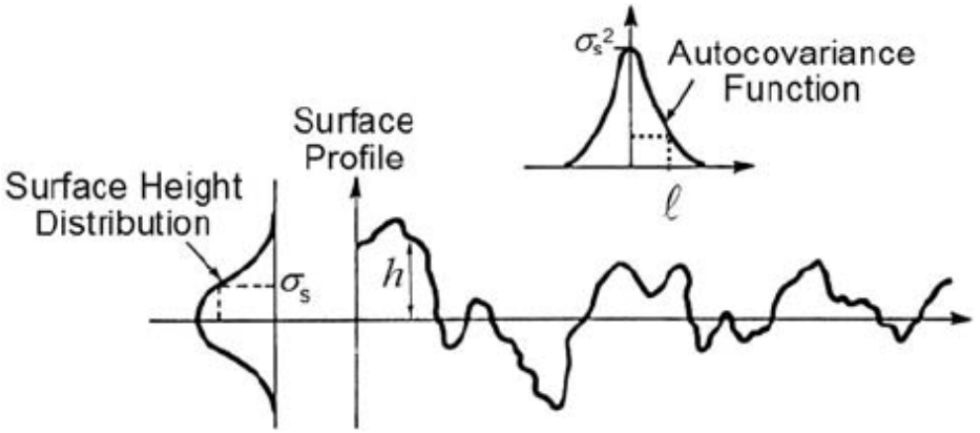

Figure 2.2: A rough surface illustrated. The height deviation h is shown as the distance from the mean height, indicated with the horizontal line, which also indicates the direction r along the surface. The surface height distribution is illustrated as a Gaussian on the left, with the RMS roughness σ_s as the standard deviation. The corresponding ACV function is illustrated on the top, with the correlation length l indicated. Credit: Krywonos et al. 2011 [21].

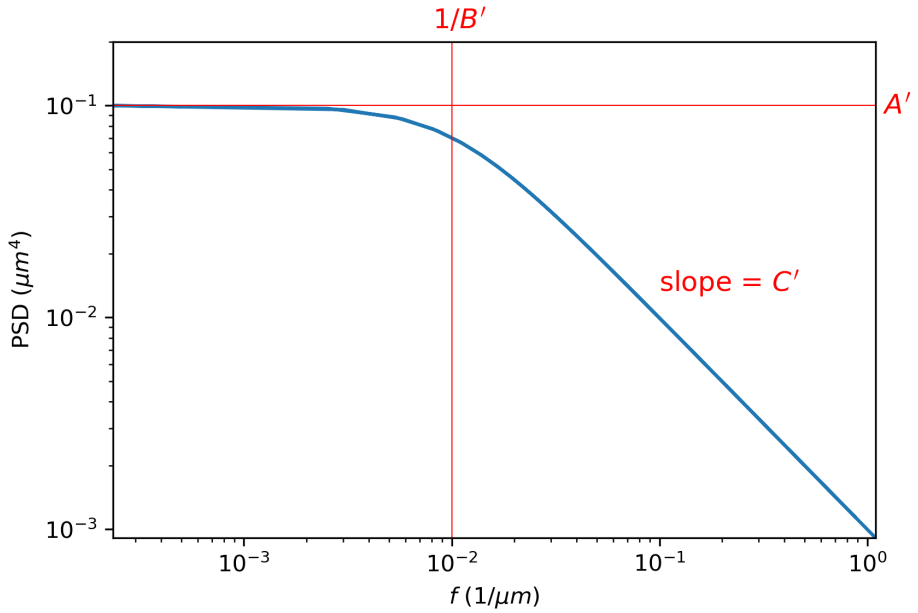

Figure 2.3: ABC model of the surface PSD as a function of the spatial frequency f. The parameters used here are $A' = 0.1\ \mu m^4$, $B' = 1/0.01\ \mu m$, and $C' = 1$, corresponding to $\sigma_s \approx 56 \mu m$.

2.2.2.1 History

The Kirchhoff method, also known as the Kirchhoff Approximation or tangent plane approximation, was one of the first attempts to model the scattering of light from a rough surface. This analytical approach uses physical optics and approximates each point of the surface as a plane tangent to that point, such that the reflection of light is considered to be locally specular [31]. The expression for the final field with this model is complicated and no analytical solution has been found without further approximations.

Many other scattering models have originated from the Kirchhoff Approximation, but each of them has its limitations [8]. For example, the Rayleigh-Rice (RR) model is a model based on vector perturbation theory that gives a good description of smoother surfaces. However, since it assumes the roughness to be a perturbation of a perfectly smooth surface, it has the requirement that the roughness is much smaller than the wavelength of the incident light, so it cannot be used for rougher surfaces [20]. The Beckmann-Kirchhoff (BK) model is based on the tangent plane approximation and assumes a Gaussian distribution of the surface's properties. It can be used for smooth and rough surfaces and describes small incidence and scattering angles with good accuracy, but it is not valid for big incidence and scattering angles.

Andrey Krywonos [21] developed the Modified Beckmann-Kirchhoff (MBK) and the Generalized Harvey-Shack (GHS) model to correct for the various limitations of previous models. The MBK model is valid for either very smooth or very rough surfaces. Although we are interested in studying smooth surfaces, the MBK model assumes a Gaussian surface PSD, which is not often the case for the polished surfaces of our interest. The Generalized Harvey-Shack (GHS) model is one of the most complete models to date, without assumptions on the PSD, and valid for both smooth and rough surfaces, as well as for small and large incidence and scattering angles. For this reason, we choose to work with the GHS model to fit our experimental data.

2.2.2.2 Harvey-Shack Models

The "Harvey-Shack model" is often presented in literature[13][10] as merely a parametrization of the RR perturbation theory, in which the BRDF is proportional to the PSD of the roughness of the sample's surface.

To demonstrate this, we start by considering a plane surface. The coordinates are such that the x-y plane corresponds to the plane of the surface of the sample. We use spherical coordinates as indicated in Fig. 2.4, where $\phi \in [0, 2\pi]$ and $\theta \in [0, \pi/2]$. To describe the variables normalized by the wavelength, we write them with a hat. For example, $\hat{x} = x/\lambda$. In this text, when referring to the direction of scattered light, a subscript s will be used. For example, θ_s refers to the angle θ of scattered light. Similarly, a subscript i refers to the direction of incident light and o refers to the specular reflection.

The RR model is given by

$$BRDF(\theta_i; \theta_s, \phi_s) = \frac{4\pi^2 \Delta n^2}{\lambda^4} \cos\theta_i \cos\theta_s Q S_2(\hat{f}_x, \hat{f}_y), \tag{2.16}$$

where Q is the polarization-dependent reflectance of the surface, Δn is the dif-

ference in refractive index between the material of the scatterer and the medium in which it is located, λ is the wavelength and S_2 is the 2-dimensional PSD of the surface. Here the value of ϕ_i is set to zero for simplification. Assuming isotropy of the surface, changing the value of θ_i simply rotates the BRDF around the z-axis without changing its shape.

The surface spatial frequencies of interest $\hat{f}_x$ and $\hat{f}_y$ can be found by treating the surface as a grating and using the hemispherical grating equation [26]:

$$\hat{f}_x = \frac{\sin\theta_s\cos\phi_s - \sin\theta_i}{\lambda} \quad \hat{f}_y = \frac{\sin\theta_s\sin\phi_s}{\lambda}. \tag{2.17}$$

Using the ABC model for S_2 (Eq. 2.13), we have

$$BRDF(\theta_i;\theta_s,\phi_s) = \frac{4\pi^2\Delta n^2}{\lambda^4}\cos\theta_i\cos\theta_s Q \frac{A'}{\left[1+\left(B'\sqrt{\hat{f}_x^2+\hat{f}_y^2}\right)^2\right]^{C'/2}}, \tag{2.18}$$

which can be parametrized as

$$BRDF(\theta_i;\theta_s,\phi_s) = b\left[1+\left(\frac{\sqrt{f_x^2+f_y^2}}{l}\right)^2\right]^{s/2}, \tag{2.19}$$

with

$$b = \frac{4\pi^2\Delta n^2 Q A'}{\lambda^4}$$
$$l = \frac{\lambda}{B'}$$
$$s = -C'$$

and

$$f_x = \sin\theta_s\cos\phi_s - \sin\theta_i, \qquad f_y = \sin\theta_s\sin\phi_s. \tag{2.20}$$

The term $\cos\theta_i\cos\theta_s$ is called the "obliquity factor", and it is usually neglected. Although this has been attributed to the effect of dust contamination on experimental data [13], the reason why it is neglected is still unclear, so understanding the effect and relevance of the obliquity factor would require further experimental data on clean surfaces. For the purposes of this thesis, the obliquity factor was ignored.

In the plane of incidence, $\phi = 0$ or $\phi = \pi$, depending on which side we are looking at with respect to the surface's normal. Using this in 2.17 gives:

$$f_y = 0 \tag{2.21}$$

$$f_x = \begin{cases} \sin\theta_s - \sin\theta_i, & \phi = 0 \\ -\sin\theta_s - \sin\theta_i, & \phi = \pi \end{cases} \tag{2.22}$$

Since $-\sin(\theta) = \sin(-\theta)$, instead of using two different expressions depending on the value of ϕ, we can simply use $f_x = \sin\theta_s - \sin\theta_i$ in a system of coordinates in which θ is negative on the side where $\phi = \pi$ and positive where $\phi = 0$.

The expression for the BRDF in the plane of incidence becomes

$$BRDF(|\sin(\theta_s) - \sin(\theta_i)|) = b\left[1 + \left(\frac{|\sin(\theta_s) - \sin(\theta_i)|}{l}\right)^2\right]^{s/2}. \tag{2.23}$$

When plotting the value of the BRDF against $|\sin(\theta_s) - \sin(\theta_i)|$ in log scale, the plot has the shape shown in Fig. 2.5. Similarly to the ABC model of the PSD, the parameters b, l, and s indicate the maximum value of the BRDF, the roll-off, and the slope, respectively.

Eq. 2.23 is what is typically presented in the literature as the "Harvey-Shack model". The Harvey-Shack model, however, is not a parametrization of the RR model. Although the Harvey-Shack model approximated for smooth surfaces can be parametrized in the same way as in Eq. 2.23, without certain approximations, they differ.

The original Harvey-Shack (OHS) model was developed by James E. Harvey and Roland V. Shack in 1976 as a linear systems diffraction BRDF [18]. This model describes the scatter with a surface transfer function, relating the scattered field to the input field as a function of the surface's properties. It treats the scatter as diffraction phenomena resulting from phase variations of light due to its interactions with surface imperfections. For this reason, it does not differentiate between surface scattering and scattering due to particulates on the surface [8], since they are both treated as part of the surface roughness.

The OHS model has the advantages that we do not necessarily need to choose a Gaussian function to describe the surface PSD and that it can be applied to both smooth and rough surfaces, but it is limited to small incidence and scattering angles due to assumptions made in the derivation of the expression for the transfer function. The Modified Harvey-Shack model was an improvement of the OHS model, being valid for large incidence angles. However, it was still limited to scattering angles close to specular reflection.

In 2011, Krywonos developed the GHS model that allows for big scattering and incidence angles, smooth and rough surfaces, and different forms of the ACV function. Details on the derivation of the GHS model can be found in [20], and the following subsection presents an overview of this model and shows how it can be approximated with the expression from Eq. 2.23.

2.2.2.3 The Generalized Harvey-Shack Model

The GHS model uses the same system of coordinates shown in Fig. 2.4, and a parametrization with direction cosines:

$$\alpha = \sin(\theta)\cos(\phi), \qquad \beta = \sin(\theta)\sin(\phi), \qquad \gamma = \cos(\theta).$$

The BRDF is given by:

$$BRDF(\alpha_s, \beta_s; \gamma_i, \gamma_s) = R\ \mathrm{ASF}(\alpha_s, \beta_s; \gamma_i, \gamma_s), \tag{2.24}$$

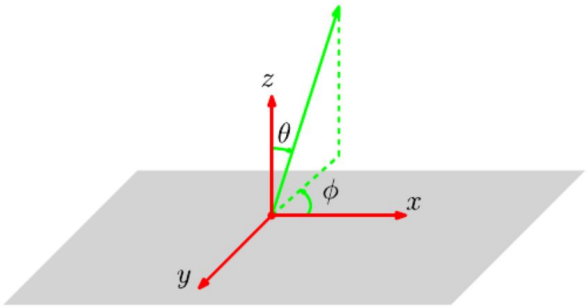

Figure 2.4: System of coordinates used for Rayleigh-Rice and Harvey-Shack methods.

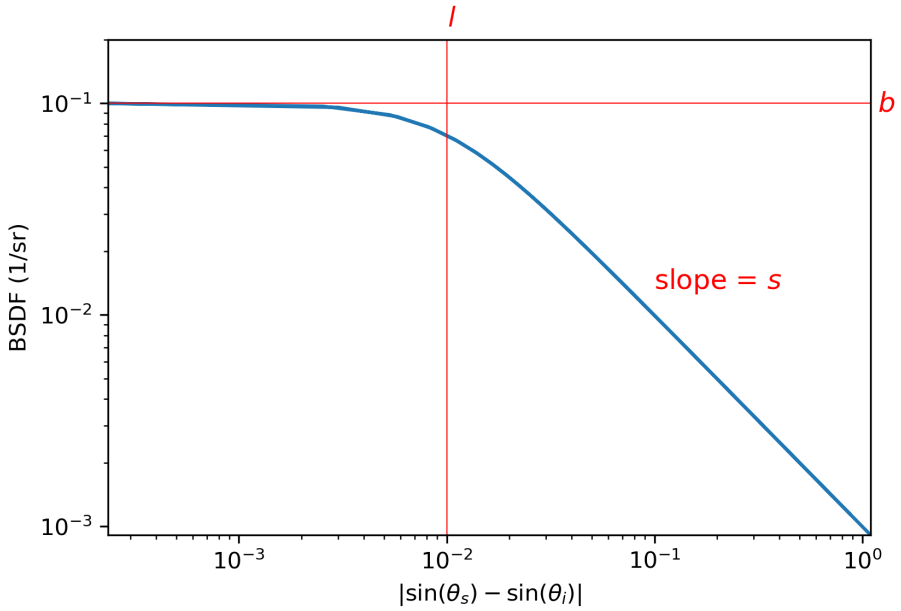

Figure 2.5: BRDF from Rayleigh-Rice model in incidence plane for b=0.1 sr^{-1}, l=0.01, s=-1.

where ϕ_i was assumed to be 0, R is the power reflectance of the surface and ASF stands for *angle spread function*. It is given by a shifted two-dimensional Fourier transform of the transfer function $H(\hat{x}, \hat{y}; \gamma_i, \gamma_s)$:

$$\mathrm{ASF}(\alpha_s, \beta_s; \gamma_i, \gamma_s) = \mathcal{F}\{H(\hat{x}, \hat{y}; \gamma_i, \gamma_s)\exp(-i2\pi\beta_o\hat{y})\} \mid_{\alpha=\alpha_s, \beta=\beta_s} . \tag{2.25}$$

The Fourier transform function can be written as

$$\mathcal{F}\{H(\hat{x}, \hat{y})\}(\alpha, \beta) = \int_{-\infty}^{\infty}\int_{-\infty}^{\infty} H(\hat{x}, \hat{y})e^{-i2\pi(\hat{x}\alpha+\hat{y}\beta)}d\hat{x}d\hat{y}. \tag{2.26}$$

The transfer function is given by:

$$H(\hat{x}, \hat{y}; \gamma_i, \gamma_s) = \exp\{-[2\pi\hat{\sigma}_{rel}(n_1\gamma_i \pm n_2\gamma_s)]^2[1 - C_s(\hat{x}, \hat{y})/\sigma_s^2]\}, \tag{2.27}$$

where n_1 is the refraction index of the external medium, n_2 the refractive index of the material of the scatterer. The minus sign is used if $n_2 < n_1$ and the plus sign is used if $n_1 < n_2$. Although the transfer function can be applied to both reflected and transmitted scattering, the steps described here consider only the reflected part of the scattering. We consider a mirror surface immersed in air, so $n_1 = -n_2 = 1$ and the term $n_1\gamma_i \pm n_2\gamma_s$ becomes $\gamma_i + \gamma_i$. σ_{rel} is the so-called relevant roughness.

The relevant roughness represents the part of the RMS roughness that contributes to the BRDF, because scattering at more than 90° from the surface normal does not contribute to the diffused light in reflection. The waves that do contribute to it satisfy the condition $\alpha_s^2 + \beta^2 < 1$. Combining this with the grating equation from Eq. 2.17, we see that the spatial frequencies that contribute to the BRDF are inside a circular boundary of radius $1/\lambda$ in spatial frequency space, centered at

$$\hat{f}_o = \frac{\sin\theta_o}{\lambda}. \tag{2.28}$$

This is illustrated in Fig.2.6. The relevant roughness is defined as the square root of the integral of the surface PSD over the relevant frequency section:

$$\sigma_{rel}(\lambda, \theta_i) = \sqrt{\int_{-1/\lambda+f_o}^{1/\lambda+f_o}\int_{-\sqrt{1/\lambda^2-(f_x-f_o)^2}}^{\sqrt{1/\lambda^2-(f_x-f_o)^2}} PSD(f_x, f_y)df_xdf_y}. \tag{2.29}$$

The transfer function can also be written as

$$H(\hat{x}, \hat{y}; \gamma_i, \gamma_s) = A(\gamma_i, \gamma_s) + B(\gamma_i, \gamma_s)G(\hat{x}, \hat{y}; \gamma_i, \gamma_s). \tag{2.30}$$

$A(\gamma_i, \gamma_s)$ describes the energy contained in the specular reflection:

$$A(\gamma_i, \gamma_s) = \exp\{-\left[2\pi(\gamma_i + \gamma_s)\hat{\sigma}_{rel}\right]^2\}, \tag{2.31}$$

$B(\gamma_i, \gamma_s)$ describes the energy contained in the scattered radiation:

$$B(\gamma_i, \gamma_o) = 1 - A(\gamma_i, \gamma_o), \tag{2.32}$$

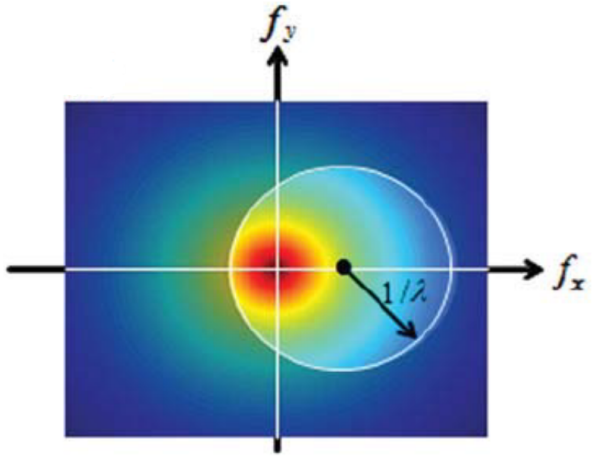

Figure 2.6: Relevant section of the PSD indicated in spatial frequency space. The colors indicate the shape of the PSD, which in this case is radially symmetric and centered at $\hat{f}_x = \hat{f}_y = 0$. λ is the wavelength of the incident light and the circle of radius $1/\lambda$ indicates the boundary of the relevant section, centered at $\hat{f}_x = \sin\theta_o/\lambda$. Image Credit: Krywonos et al. (2011)[21]

and $G(\hat{x}, \hat{y}; \gamma_i, \gamma_s)$ describes the distribution of the scattered radiation:

$$G(\hat{x}, \hat{y}, \gamma_i, \gamma_s) = \frac{e^{-[2\pi(\gamma_i+\gamma_s)\sigma_{rel}/\sigma_s]^2 C_s(\hat{x},\hat{y})} - 1}{e^{-[2\pi(\gamma_i+\gamma_s)\hat{\sigma}_{rel}]^2} - 1}. \tag{2.33}$$

Using Eq. 2.34, the ASF can be written as

$$\mathrm{ASF}(\alpha_s, \beta_s; \gamma_i, \gamma_s) = A(\gamma_i, \gamma_o)\delta(\alpha_s, \beta_s - \beta_o) + K(\gamma_i)S(\alpha_s, \beta_s; \gamma_i, \gamma_s). \tag{2.34}$$

where the Dirac-delta function describes the single reflection peak at the angle of specular reflection. $S(\alpha_s, \beta_s; \gamma_i, \gamma_s)$ is the scattering function and is given by

$$S(\alpha_s, \beta_s; \gamma_i, \gamma_s) = B(\gamma_i, \gamma_s)\mathcal{F}\{G(\hat{x}, \hat{y}, \gamma_i, \gamma_s)e^{-i2\pi\beta_o\hat{y}}\}. \tag{2.35}$$

$K(\gamma_i)$ is a renormalization constant, which compensates for the cases in which diffraction at angles more than 90° from the surface normal occurs and does not contribute to the TIS. It thus ensures that the integral of $S(\alpha_s, \beta_s; \gamma_i, \gamma_s)$ is equal to the real and measurable value of the TIS. $K(\gamma_i)$ is given by

$$K(\gamma_i) = B(\gamma_i, \gamma_o)\left(\int_{-1}^{1}\int_{-\sqrt{1-\alpha_s^2}}^{\sqrt{1-\alpha_s^2}} S(\alpha_s, \beta_s; \gamma_i, \gamma_s)\, d\alpha_s d\beta_s\right)^{-1} \tag{2.36}$$

This expression for the ASF does not have a closed-form solution and is very computationally expensive since a two-dimensional Fourier transform needs to be performed for each scattering angle. This can be greatly simplified when using a smooth-surface approximation.

When the surface is very smooth, the rms roughness becomes much smaller than the wavelength of the incident light, meaning $\hat{\sigma}_{rel} << 1$. We can then expand equations 2.31, 2.32 and 2.33 for small arguments and use the approximations:

$$A(\gamma_i, \gamma_s) \approx 1 - [2\pi\hat{\sigma}_{rel}(\gamma_i + \gamma_s)]^2, \tag{2.37}$$

$$B(\gamma_i, \gamma_s) \approx [2\pi\hat{\sigma}_{rel}(\gamma_i + \gamma_s)]^2, \tag{2.38}$$

$$G(\hat{x}, \hat{y}) \approx \frac{C_s(\hat{x}, \hat{y})}{\sigma_s^2}. \tag{2.39}$$

The expression in Eq. 2.23 is obtained by considering only the scattered energy and ignoring the specular reflection, since the BRDF is usually defined as such. We thus ignore the first term in Eq.2.34. This gives:

$$\mathrm{ASF}(\alpha_s, \beta_s; \gamma_i, \gamma_s) = K(\gamma_i) S(\alpha_s, \beta_s; \gamma_i, \gamma_s). \tag{2.40}$$

With the approximations, the expression in Eq.2.35 becomes:

$$S(\alpha_s, \beta_s; \gamma_i, \gamma_s) = [2\pi\hat{\sigma}_{rel}(\gamma_i + \gamma_s)]^2 \ \frac{1}{\sigma_s^2} \mathcal{F}\{C_s(\hat{x}, \hat{y}) e^{-i2\pi\beta_o\hat{y}}\}, \tag{2.41}$$

with

$$\mathcal{F}\{C_s(\hat{x}, \hat{y}) e^{-i2\pi\beta_o\hat{y}}\}(\alpha_s, \beta_s) = \frac{1}{2\pi} \int_{-\infty}^{\infty} \int_{-\infty}^{\infty} C_s(\hat{x}, \hat{y}) e^{-i2\pi(\alpha_s\hat{x} + (\beta_s + \beta_o)\hat{y})} d\hat{x} d\hat{y}. \tag{2.42}$$

This integral is a Fourier transform where the frequency variable in the y-direction is translated: instead of β_s it is $\beta_s + \beta_o$, or $\beta_s - \beta_i$. This results in a shift in the scattered radiance in direction cosine space [20]. Since the form of the BRDF remains the same, Eq.2.42 is then simply equivalent to the Fourier transform of the ACV function, which is the PSD.

Therefore we have:

$$\mathrm{ASF}(\gamma_s, \gamma_i; \hat{f}_x, \hat{f}_y) = [2\pi\sigma_{rel}(\gamma_i + \gamma_s)]^2 \ \frac{K(\gamma_i)}{\lambda^4 \sigma_s^2} PSD(\hat{f}_x, \hat{f}_y) \tag{2.43}$$

and the scattering function becomes proportional to the surface PSD function, which is similar to the RR model (2.16). Substituting this expression for the ASF in Eq. 2.24, and writing the PSD using the ABC model, we have:

$$BRDF(\gamma_i, \gamma_s; f) = RK(\gamma_i) \frac{[2\pi\sigma_{rel}(\gamma_i + \gamma_s)]^2}{\lambda^4 \sigma_s^2} \frac{A'}{\left[1 + \left(B' \sqrt{\hat{f}_x^2 + \hat{f}_y^2}\right)^2\right]^{C'/2}}. \tag{2.44}$$

For a certain angle of incidence, we can parametrize this as:

$$\begin{aligned} b &= RK(\gamma_i) \frac{[2\pi\sigma_{rel}]^2}{\lambda^4 \sigma_s^2} A', \\ l &= \frac{\lambda}{B'}, \\ s &= -C'. \end{aligned} \tag{2.45}$$

The final expression for the GHS model of the BRDF with the smooth-surface approximation is then:

$$BRDF(\theta_s, \phi_s, \theta_i) = b(\cos\theta_i + \cos\theta_s)^2 \left(1 + \frac{\mid f_x^2 + f_y^2 \mid}{l^2}\right)^{s/2},$$
$$f_x = \sin\theta_s\cos\phi_s - \sin\theta_i, \qquad f_y = \sin\theta_s\sin\phi_s. \tag{2.46}$$

Where ϕ_i was assumed to be zero. The obliquity factor, in this case, is $(\cos\theta_i + \cos\theta_s)^2$. It has been discovered [18] that the obliquity factor in the RR model is actually an approximation of this. In the RR theory, there is an assumption that the wavelength of the scattered light is shorter than the surface autocovariance length, which leads to the approximation in the obliquity term. This term is again neglected due to the aforementioned reasons.

The BRDF then assumes the same form as the expression in Eq. 2.19, derived from the RR theory. In the plane of incidence, it is again more easily described in a system of coordinates in which $\theta \in [-\pi/2, \pi/2]$.

Fig. 2.7a shows an example of the BRDF computed with the GHS model. Fig 2.7b shows the same function in the plane of incidence.

For calculating the TIS, the BRDF model is integrated over one hemisphere. This is easy to do computationally, using the GHS model and integrating numerically in θ from 0 to $\pi/2$ and in ϕ from 0 to 2π. For normal incidence, the TIS can be calculated analytically using the expression [13]:

$$TIS = \frac{2\pi b}{l^s(s+2)}\left[(1+l^2)^{\frac{(s+2)}{2}} - (l^2)^{\frac{(s+2)}{2}}\right], \tag{2.47}$$

where b, l and s are the fitting parameters of the GHS model.

2.3 Scattering due to Particulates

When dust particles are present on the surface of the material, the total scattering becomes a combination of both the scattering due to surface roughness and the one due to the interaction of light with the particles. Mie scatter theory, named after Gustav Mie, describes the scattering due to homogeneous and spherical particles. Although dust particles are not typically spherical, it has been shown [25] that making the assumption that all particles are spheres often leads to a good approximation of the resulting BSDF.

According to Mie's model, the intensity and angular distribution of scattered light from a particle are proportional to the relative refractive index m and to a parameter x, given by

$$x = \frac{\pi \mathrm{Re}(N) D}{\lambda}, \tag{2.48}$$

where N is the complex refractive index of the particle, D is the particle's diameter, and λ is the wavelength of the incident light.

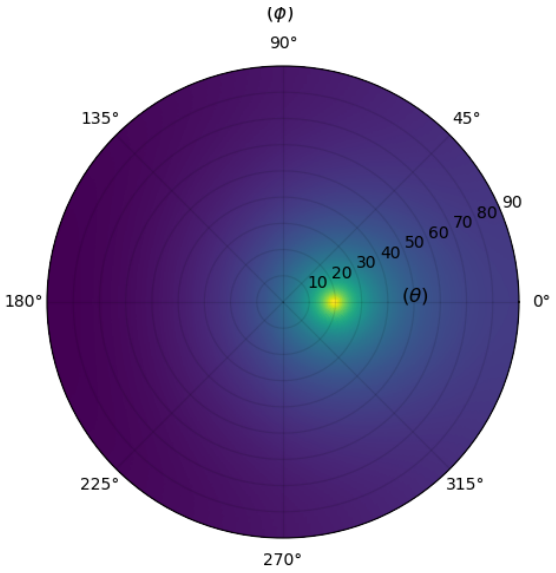

(a) Out-of-plane function.

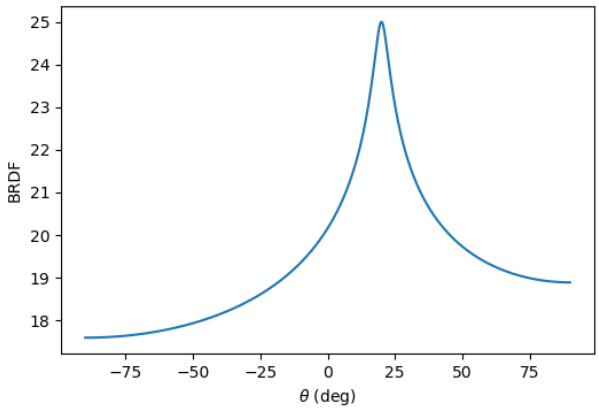

(b) In-plane function.

Figure 2.7: BRDF from GHS model with an angle of incidence $\theta_i = 20°$ and parameters $b = 0.8$, $l = 0.04$, and $s = -0.1$.

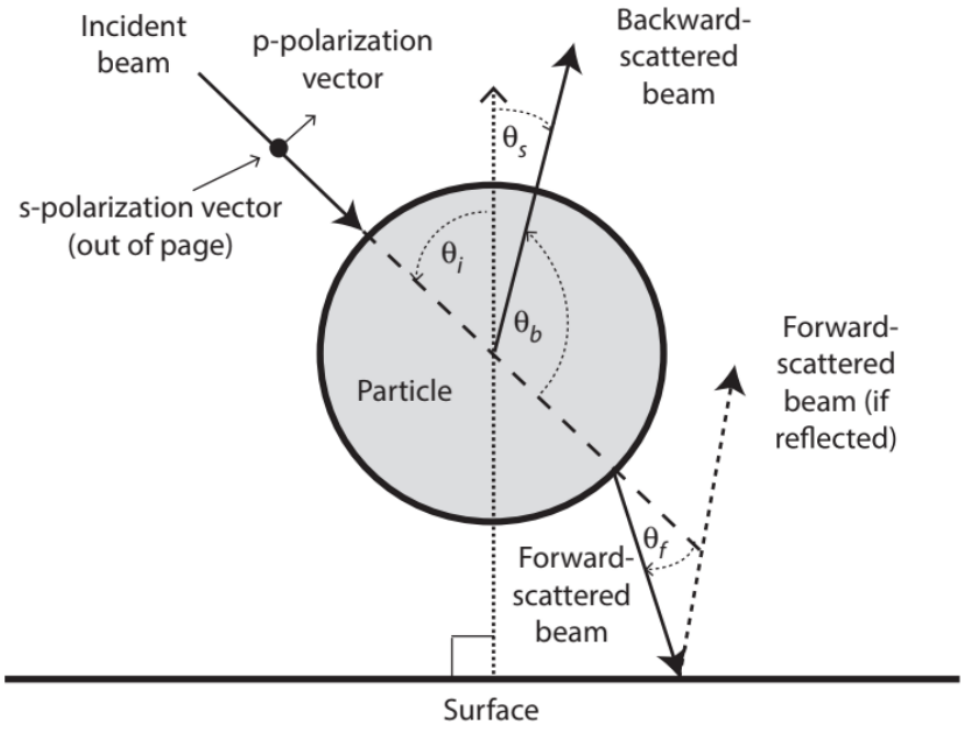

Figure 2.8: Mie scattering of a light beam as it interacts with a particle on a surface. Image source: [13].

m is given by

$$m = \frac{N}{\mathrm{Re}(N_m)}, \tag{2.49}$$

where N_m is the refractive index of the media in which the particle is located. The scattering is most intense the closer to the direction of propagation of the incident beam and its shape is also dependent on the polarization of the light beam. Presenting the full Mie model is beyond the scope of this thesis, but it can be found in Mie's original paper in [22].

When the particles lie on a surface, the observed BRDF is formed by the light scattered by the particle at an angle θ_b (backward-scattering), and the light that is transmitted through the particle at an angle θ_f and is then reflected by the surface (forward-scattering). This is illustrated in Fig.2.8

For a surface with N particulate contaminants, the BRDF is given by

$$\begin{aligned} BRDF(\theta_s) = &\frac{1}{(2\pi/\lambda)^2 \cos\theta_s} \sum_{i=1}^{N} f(D_i) \\ &\times \left[\frac{RI_s(D_i, \theta_f) + RI_p(D_i, \theta_f) + I_s(D_i, \theta_b) + I_p(D_i, \theta_b)}{2} \right], \end{aligned} \tag{2.50}$$

where λ is the wavelength of the incident light, θ_s is the scattering angle with respect to the normal of the scattering surface, D_i is the diameter of the ith particle, $f(D_i)$ is the density of particles with diameter D_i, R is the surface reflectance, and $I_s(D_i, \theta)$ and $I_p(D_i, \theta)$ are the intensities of s-polarized and p-polarized scattered light at the given scattering angle θ, respectively.

Despite the complexity of the theory, Mie scattering can be useful in case one is interested in studying the dimensions of the particles present in a certain medium. By using wavelengths comparable to the size of the particles, the shape of the BRDF gives information on the diameter of contaminants.

When the size of the particle is much smaller than the wavelength (x smaller than ≈ 0.1), the scattering is more easily described with the Rayleigh model. This model assumes that particles are molecules that absorb the incoming light by exciting an electron and immediately re-emit it with the same energy [6]. It has a strong dependence on the wavelength, with the scattering intensity proportional to $1/\lambda^4$. This means that light with a shorter wavelength is scattered more than light with longer wavelengths. Unlike Mie scattering, Rayleigh scattering generates a BSDF that is symmetric in forward and backward directions (and isotropic for specifically p-polarized light) [13], and the scattered radiation is more distributed across different directions. This is illustrated in Fig. 2.9.

Rayleigh scattering does not have a dependence on the diameter of the particle, like in the case of Mie scattering. The BRDF due to Rayleigh scattering assumes a simple form in which the intensity of the scattering is proportional to the number of particles (and other quantities), so this model is preferable when we are interested in describing the scattering due to small particles.

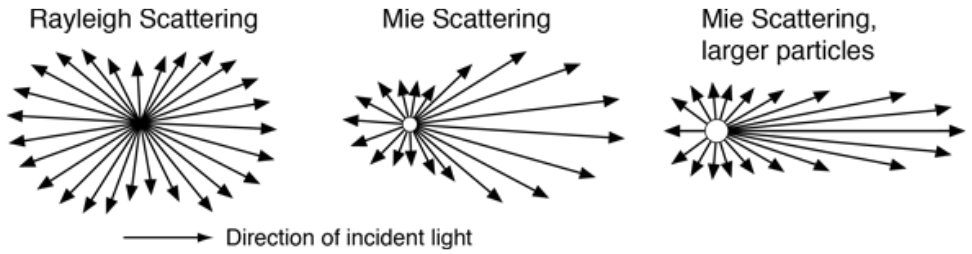

Figure 2.9: Mie scattering and Rayleigh scattering from a particle. The direction of scattered light is indicated with arrows, whose length indicates the intensity. Image source: Hyperphysics [19]

3 Instruments

We use two instruments to measure scattered light from a sample: a scatterometer, which measures the BSDF in the plane of incidence, and an integrating sphere, which measures the TIS. During the work reported in this thesis and as part of it, these two instruments that were originally hosted in different laboratories were combined in an upgraded setup hosted in a clean room in the Departimento di Fisica e Astronomia

(DFA) of the University of Padua. This allows us to easily make subsequent measurements of the same sample, in the same conditions, using each of the instruments. This way, each sample can be fully characterized and the two instruments can be more directly cross-checked.

3.1 Scatterometer

A scatterometer allows us to infer the BSDF of a sample by measuring the amount of light scattered at each angle θ_s from the surface normal of the sample along the plane of incidence, as the sample is illuminated with a laser beam. Our scatterometer consists of a laser line, a sample holder, and a photodiode. The beam of a laser source is directed towards a sample supported by a sample holder: the specular reflected and transmitted light is dumped while a high sensitivity photodetector that can be rotated around the sample at a radius of ≈ 30 cm measures the scattered light at small angular intervals.

Recalling Eq. 2.6, and under the assumption that all the light scattered from the illuminated point on the sample is seen by the detector, the BSDF of a sample can be measured in the scatterometer using the formula:

$$BSDF(\theta_i, \theta_s) = \frac{P_s(\theta_i, \theta_s)}{P_0 \cdot \Omega_d \cdot cos(\theta_s)} \tag{3.1}$$

where P_s is the power scattered by the sample and measured by the detector, P_0 the power impinging on the sample's surface, θ_i is the incidence angle, and Ω_d the solid angle of the detector as seen from the sample, assumed to be much larger than the solid angle subtended by the laser spot on the sample as seen from the detector.

The cosine term in this equation corrects for the changing projected surface area of the sample as seen from the detector. In theory, the projected surface area at $\theta_s = 90°$ is zero and so is P_s. In practice, some scattering is measured at this angle, together with background contribution. The measured BSDF then goes to infinity at 90° since the cosine in the denominator becomes 0 but the nominator does not. This effect is not physical, so it is common to represent the BSDF multiplied by $\cos(\theta_s)$.

Originally, the scatterometer was built with a simplified setup in a laboratory that is not a clean room, so it was not shielded against dust contaminants. Despite limitations, with this setup, we were able to calibrate and test the instrument before moving it to a clean room and building its more complex version. The original setup is shown in Fig. 3.1.

The laser used for this has a wavelength of 1064 nm, which is the wavelength used in current advanced detectors. The output is linearly polarized and has a nominal power of 1W; we rather measured a power of 1.2W. To be able to control this power, we use a system consisting of a half-waveplate (HWP) and a polarizing beamsplitter (PBS). The HWP has the effect of rotating the direction of polarization of the impinging light. The effect of the PBS is that of separating spatially two orthogonally polarized fields: the p-polarization is transmitted while the s-polarization is reflected. The transmitted component continues its path in the instrument reaching the sample, while the other component is sent 90° from this direction and is absorbed by a dumper (Dumper 1 in Fig. 3.1). By rotating the HWP, we change the polarization angle and thus the power we send into the system.

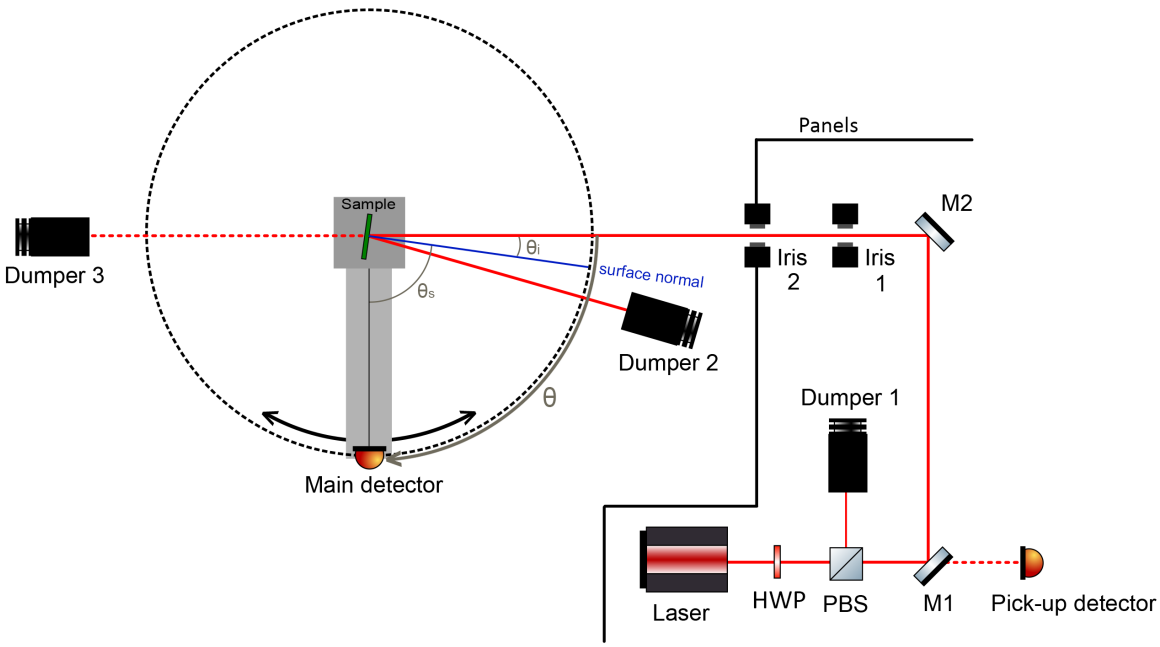

Figure 3.1: Original scatterometer setup (not to scale). HWP stands for half-waveplate, PBS stands for polarizing beam splitter, and M stands for mirror. The black line represents the cardboard panels placed around the optics.

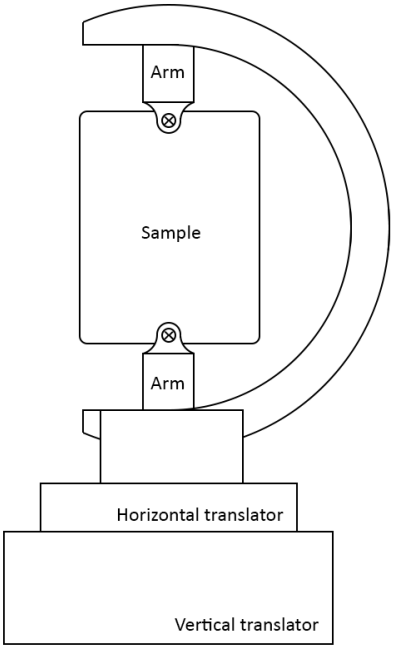

Figure 3.2: Sample holder in the scatterometer

The mirrors M1 and M2 were placed to ensure the alignment of the beam. Since the mirrors do not reflect perfectly and a small fraction of light still goes through them, this was used to measure the incident power. A pick-up detector was placed behind M1 and this was calibrated to obtain a relationship between the power it measures and the power impinging on the sample.

In order to remove unwanted contributions from diffuse laser light or ghost beams, Iris 1 and Iris 2 were placed. The laser light then reaches the sample and both the specular reflection and the directly transmitted light are absorbed by Dumper 2 and Dumper 3, respectively, as shown in 3.1. The sample is positioned at a small angle (θ_i) with respect to the impinging beam to avoid sending light back into the system and to allow separating and damping the specular reflection. This angle can be adjusted but is limited by the lateral size of the dumper that absorbs the specular reflection. Considering the dumper used in the setup of lateral size 40 mm and the available space where it could be mounted, the minimum angle in this setup is 6.5 degrees.

The sample is secured in place with a C-shaped aluminum holder of diameter ≈ 10 cm, as illustrated in Fig. 3.2. Detachable arms, which can be positioned along the C-shape, are used to secure the sample using screws. The holder is placed on two linear translators, one that moves it horizontally and one that moves it vertically on the plane parallel to the sample surface facing the impinging laser beam. Both of them are regulated with micrometers to allow for precise and controllable movement. Finally, the vertical translator is placed on a rotating platform that allows us to rotate the structure of the holder to change θ_i.

The detector, which is attached to the movable arm, is a silicon photodiode (model SM1PD1A from Thorlabs [29]) that measures the amount of received light as a voltage. It is sensitive to wavelengths between 350 nm and 1100 nm, with a sensitivity peak at 970 nm. At a wavelength of 1064 nm, it has a responsivity of 0.82 A/W. It has a diameter of 1 mm, with which we achieve an angular resolution of the scatterometer of 0.2 degrees.

The arm rotation can be controlled remotely via a Labview-based program. The program sets the starting and ending angles of the movement, the angular steps that it takes as it moves between measurements, the number of measurements made at each position and the time interval between them, and the angular position of the sample. It also saves the acquired data as the voltage registered by the photodiode. The movement of the arm is limited by the specular reflection and the direct transmission of the laser beam: to avoid damaging the detector due to the high laser power and to avoid scattering of the light beam on the surface of the detector, the initial and final positions of the arm are set to a minimum distance of about 14 degrees from the beam.

An iris and a narrowband filter are mounted in front of the photodiode such that they are both comoving with the arm. The iris is placed 10 mm away from the detector with a diameter of 2 mm. This diameter was chosen experimentally, such that the background contribution is minimized without clipping the actual signal. The narrowband filter lets through only light at 1064 ± 5 nm. This removes considerable background contributions like the thermal radiation in the room, which could saturate the detector or pollute the measurements. Other background contributions still remain, like any thermal radiation with frequency in the 1064 ± 5 nm band and scattering of the laser light on the optics, dust, and molecules in the air. The background contribution from scattering was reduced by placing black cardboard panels around the optics (indicated with a black line in Fig. 3.1).

To identify the signal amid the remaining background noise, the input laser signal is modulated as a square wave. For this, the laser power is turned on and off according to a reference signal at a frequency of 23 Hz. The signal of the scatterometer's main photodiode is firstly filtered by a lock-in amplifier at the square wave signal and then acquired. This is registered on the computer as a function of the angle θ between the arm and the incident beam. Variations in the laser power are taken into account by normalizing the data to the light power monitored by the pick-up photodiode. Other limitations are errors in the alignment of the detector with the plane of incidence, possible shadows, and electronic noise.

Rayleigh scattering from laser light on the molecules in the air originates a stray light contribution that cannot be removed (unless going under vacuum). The following subsection provides an estimate of the magnitude of this noise, which was used to explore how much its contribution is to the background noise measured with the scatterometer, and whether there are other limiting factors that could be explored.

3.1.1 Contribution of Air to BRDF measurements

When making measurements with the scatterometer, we need to take into account the contribution that we expect to have from the air in the laboratory. Before the laser light reaches the sample, it travels through air and can be scattered by the molecules.

Since the wavelength is much larger than the size of the particles, this is described by Rayleigh scattering.

A formula for the BRDF due to Rayleigh scattering on gas was derived by Asmail et al. (1994) [3], who also published a corrigendum in 1999 [4]. Starting from their derivation and adapting it to the case of our instrument, we can estimate the contribution of the air in the laboratory to the BRDF when the laser light scatters off gas.

The BRDF is calculated by using a reference sample with BRDF f_R. For this, we use the fact that the ratio between the BRDFs is equal to the ratio between the average scattered flux of the reference and of the air. This can be written as

$$\frac{f_R \cos\theta_R}{f_{air}} = \frac{\Phi_R}{\Phi_{air}}, \tag{3.2}$$

where f_{air} is the BRDF due to the air, θ_R is the angle between the sample's normal and the direction of the detector, Φ_R is the scattered flux of the reference sample, and Φ_{air} is the scattered flux of the air. The term $\cos\theta_R$ accounts for the fact that the irradiated area on the sample as viewed from the detector changes as the detector moves, so the BRDF of the sample should be scaled by this quantity.

The geometry of the problem is illustrated in Fig. 3.3. The light beam travels through the z-axis and has a cross-section A_d. The detector is at point p, which is at an angle η_0 (θ in this text) from the z-axis, and it has an area A_p. The distance from the detector to a central point O is r_0. l is the length of the beam that falls inside the detector's field of view.

From Eq. 3.1, we can write:

$$\Phi_R = f_R \Phi_I \Omega \cos\theta_R, \tag{3.3}$$

where Φ_I is the irradiance of the incident beam and Ω is the solid angle of the detector, given by A_p/r_0^2. In our case, $r_0 = 0.275m$, the length of the scatterometer's arm.

Eq. 2 in Ref.[3] gives:

$$E_p = A_d N k^4 \mid \alpha \mid^2 E_i L \tag{3.4}$$

where E_p is the irradiance at point p due to scattering of light on all air molecules inside a volume $A_d l$, N the number of gas molecules per unit volume, k the wave number, equal to $2\pi/\lambda$ with λ the wavelength of light, α the polarizability of the gas, given by $[3/(4\pi N)][(n^2-1)/(n^2+2)]$, with n the index of refraction of the gas (1.0003 for air), E_i is the irradiance of the light beam on cross-section A_d, and

$$L = \int_{-l/2}^{l/2} \frac{1}{r^2} dz, \tag{3.5}$$

with $r^2 = r_0^2 + z^2 - 2 r_0 z \cos\theta$. The angle θ is the angle that the detector makes with the incident beam.

E_p can be written as Φ_{air}/A_p, and E_i can be written as Φ_I/A_d. Eq. 3.4 then becomes:

$$\Phi_{air} = A_p N k^4 \mid \alpha \mid^2 \Phi_I L. \tag{3.6}$$

Plugging Eq. 3.6 and Eq. 3.3 into Eq. 3.2, and using $\Omega = A_p/r_0^2$, we have:

$$\frac{f_R \cos\theta_R}{f_{air}} = \frac{f_R \cos\theta_R}{r_0^2 N k^4 \mid \alpha \mid^2 L}, \tag{3.7}$$

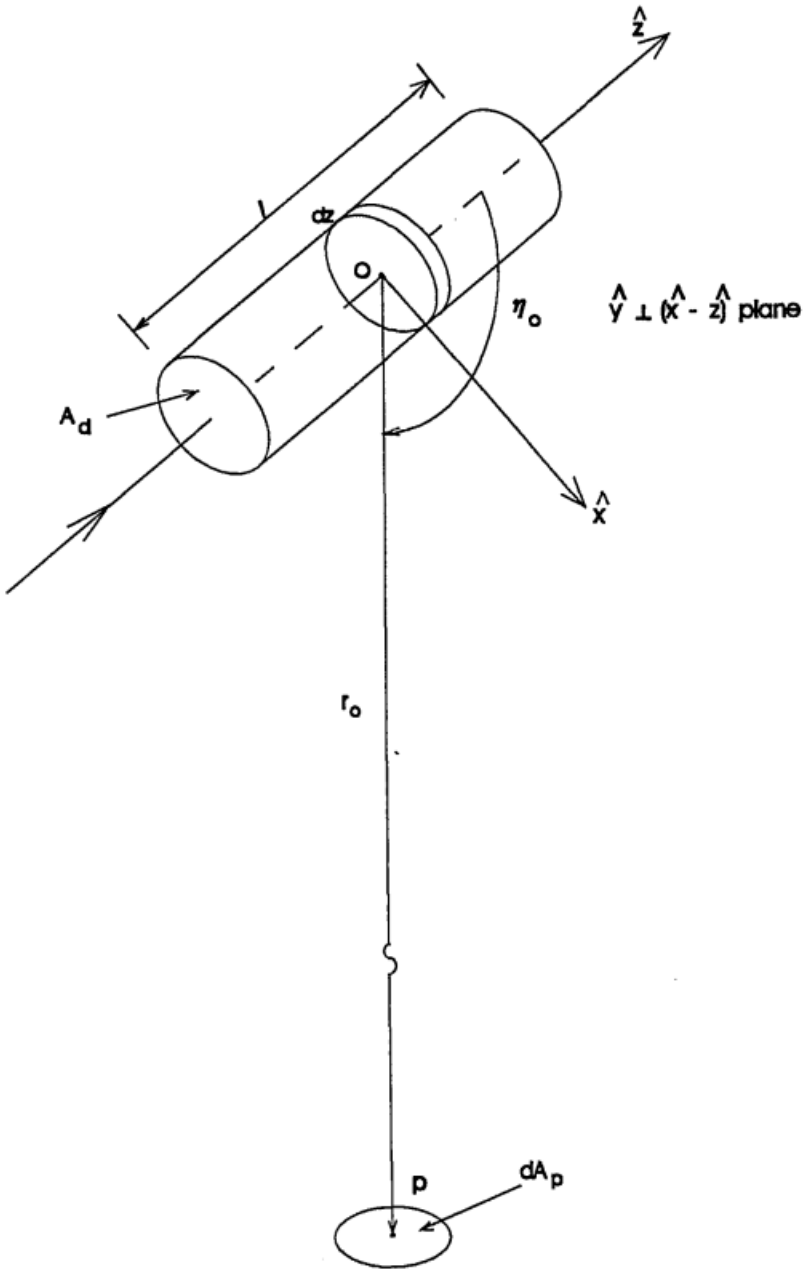

Figure 3.3: Geometry of the problem. Credit: Asmail et al. (1994)

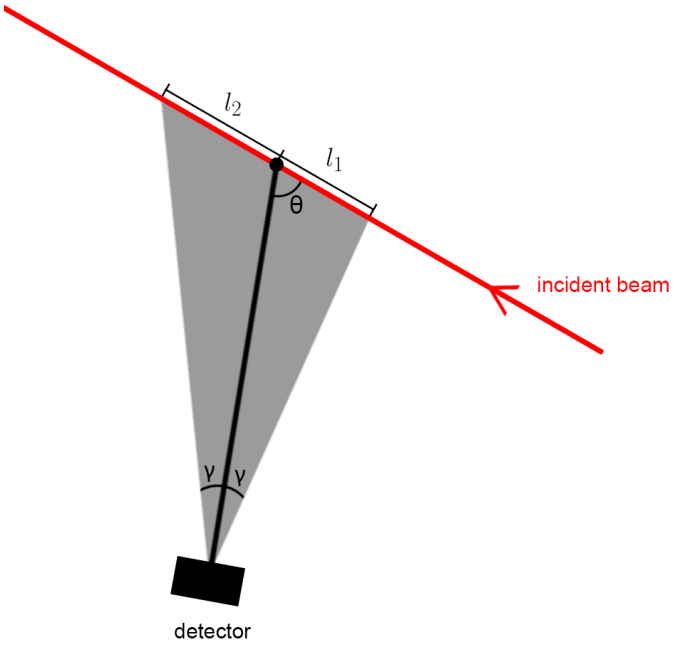

Figure 3.4: The lengths l_1, l_2 and the angles θ and γ indicated in the instrument as used in this text.

giving

$$f_{air} = r_0^2 N k^4 \mid \alpha \mid^2 L. \tag{3.8}$$

If l is very small compared to r_0, we can use $r^2 \approx r_0^2$ and L is simply equal to l/r_0^2. This gives a BRDF of

$$f_{air} = l N k^4 \mid \alpha \mid^2, \tag{3.9}$$

as Asmail et al. (1999) concluded. However, this might not be the case for our detector. Since the field of view of our detector is big (17.06 deg), when the detector is at 90 degrees with respect to the incident beam, we have $l = 0.082m$. This is about 30% of r_0. We then have to use the full form of the integral, which is not easily solvable analytically. It was instead solved numerically using the `integrate` function from the Python Scipy package.

The limits of the integral in Eq. 3.5 also come from the assumption that l is very small, so that we can consider half of l to be on the positive side of the z-axis and the other half to be on the negative side, with the center of rotation of the detector at $z = 0$. In our case we cannot assume that these limits are symmetrical, so instead of calculating the integral from $-l/2$ to $l/2$, we split the length l into two contributions, l_1 and l_2, corresponding to the length of l lying on the positive and negative sides of the z-axis, respectively. This is illustrated in Fig.3.4. We then integrate from $-l_2$ to l_1.

Using the law of sines, we can write:

$$l_1 = r_0 \frac{sin(\gamma)}{sin(\theta+\gamma)}, \qquad l_2 = r_0 \frac{sin(\gamma)}{sin(\theta-\gamma)},$$
$$l = l_1 + l_2 = r_0 sin(\gamma) \left(\frac{1}{sin(\theta+\gamma)} + \frac{1}{sin(\theta-\gamma)} \right). \tag{3.10}$$

When $\theta+\gamma = \pi$ or when $\theta-\gamma = 0$, the value of l goes to infinity. In reality, this does not happen because the beam is absorbed by a dumper at a distance $d \approx r_0$ from the center of rotation of the detector and is limited by the laser output on the other side, while also being partially blocked from the detector's field of view by the structure of the instrument and other components. We, therefore, set a maximum value of r_0 for l_1 and l_2. For each angle θ, the values of l_1 and l_2 are calculated and the integral is computed, so we have L as a function of θ.

Another problem is that, with this integration, for an angle $\theta = 0$ or $\theta = 180°$, using $l_1 = l_2 = r_0$, the integral diverges to infinity. This is because the $1/r^2$ term in L accounts for attenuation due to the distance from the beam to the detector, but the distance in this case is 0. At very small distances, this expression is not valid. Since the detector never reaches such small angles and stops at a certain distance from the laser beam to avoid unwanted scattering, the simulation was also limited to those angles. The minimum angular distance from the laser beam reached by the detector is $\Delta\theta = 13.5°$, which is considered safe with respect to clipping in the old scatterometer setup. The BSDF was then calculated for $13.5° < \theta < 166.5°$.

N can be estimated using the ideal gas law, assuming a pressure of 1 atm and a temperature of $25°C$, which gives $N = 2.45 \cdot 10^{25} m^{-3}$. The calculations were performed for a wavelength $\lambda = 1064$ nm.

Fig. 3.5 shows the resulting BRDF as a function of the angle θ. The changes in slope at around $\theta = 20°$ and $\theta = 160°$ are due to the maximum values imposed on l_1 and l_2. Fig. 3.6 shows how much this computation changes using the approximation by Asmail et al. (1999) for small l. We see that the difference increases for very small and very big angles, which is what is expected since l increases as we move away from $\theta = 90°$. However, even at the extreme angles, the difference is small, with a maximum of about 7% and significantly smaller at most angles. Considering that the estimation without the approximation by Asmail et al. (1999) was still based on many assumptions and is therefore not very precise, the approximation can be considered suitable for the case of our instrument.

This gives a contribution in the order of $10^{-8} sr^{-1}$, which is the same order of magnitude as the background measured with the scatterometer in the old setup, indicating that this is probably the most limiting noise. Fig 3.7 shows the predicted BSDF due to Rayleigh scattering together with a few background measurements. The background signal is about an order of magnitude higher when measured with the sample holder in place, indicating a contribution due to scattering on the surface of the holder. The height at which the holder is placed also contributes to the variation in the background signal. The decrease at around 150° is due to a shadow created by one of the rods supporting the arm. Since the BRDF of the background is generally at least two orders of magnitude lower than that of the samples, it is usually neglected.

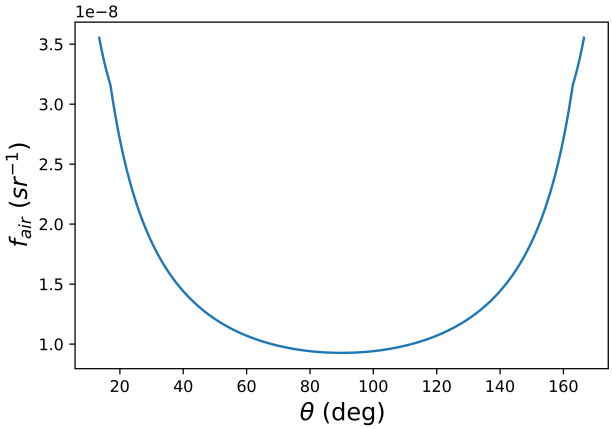

Figure 3.5: BRDF due to air between $\theta = 13.5°$ and $\theta = 166.5°$

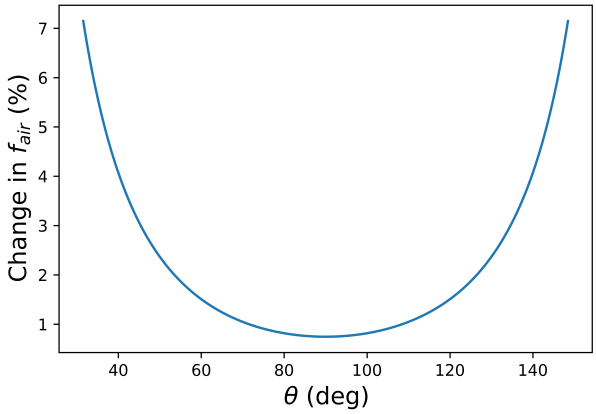

Figure 3.6: Change in the BSDF of the air due to approximation used by Asmail et al (1999) as a function of the detector angle with respect to the laser beam. Calculated as $(f_{approx} - f_{air}) \cdot 100/f_{air}$, where f_{approx} is the approximated BSDF and f_{air} is the BSDF without the approximation.

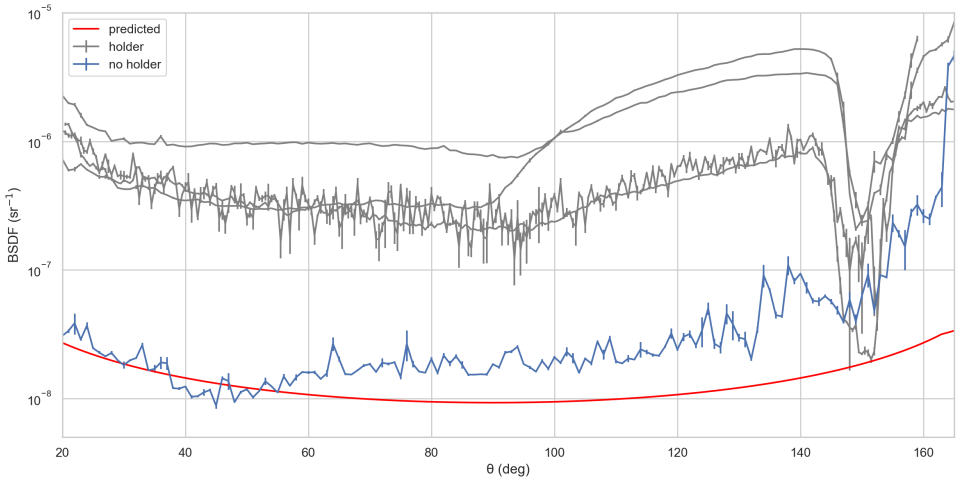

Figure 3.7: Background measurements with the scatterometer compared to the prediction due to Rayleigh scattering.

Using Eq. 3.9 for wavelengths 532 nm and 1550 nm, which are included in the new version of the scatterometer, results in a BSDF in the order of $10^{-7}sr^{-1}$ and $10^{-9}sr^{-1}$, respectively. This estimation, however, was made only for molecules in the air, like hydrogen and nitrogen. When dust is taken into consideration, we do not have necessarily Rayleigh scattering. Most likely, we have Mie scattering due to the greater sizes of these particles. The contributions due to gas molecules and due to dust particles should be added together for a final estimation of the background signal.

3.2 Integrating Sphere

The integrating sphere measures the entire amount of scattered light from the sample in one hemisphere, i.e., the TIS. It is illustrated in Fig. 3.8 (model 4P4 from Thorlabs [29]). The integrating sphere can measure both transmitted radiation and reflected radiation, depending on where the sample is placed. For reflection measurements, the sample is placed behind the opening at the back of the sphere and the two openings in the front are used for the incident beam and the specular reflection. These two openings are at an 8° angle from the normal of the sample, allowing the separation of the reflected beam from the incoming one. For transmission measurements, the sample is positioned in front of the opening for the incoming beam. The inside of the sphere is made of a diffusive material so that any light that impinges on it is reflected uniformly in all directions. A photodiode is faced to the internal side of the sphere and measures the portion of the diffused light that impinges on it as an electric current.

At the beginning of the work reported in this thesis, the integrating sphere was located in a clean room at the Laboratori Nazionali di Legnaro of Istituto Nazionale di Fisica Nucleare. Then, also as part of this work, it was integrated with the scat-

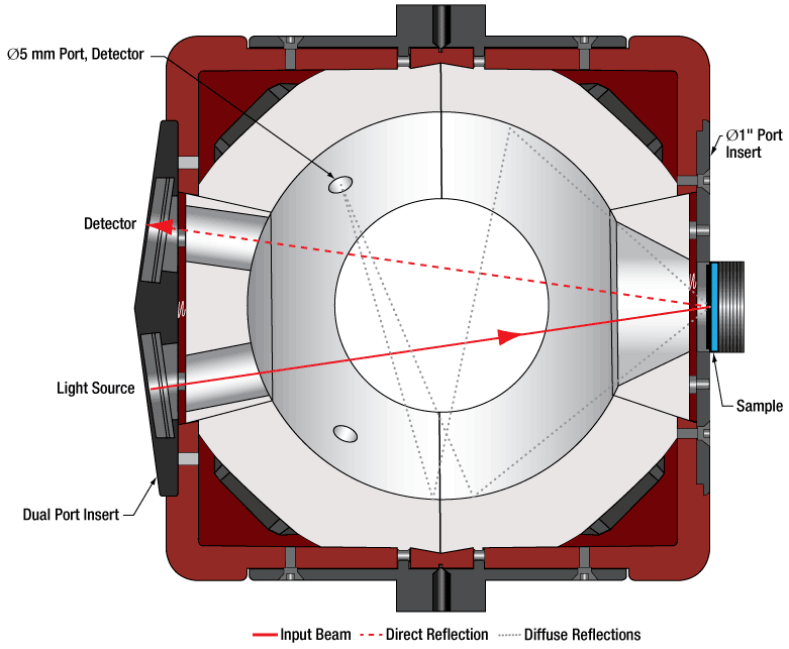

Figure 3.8: Integrating Sphere. Image credit: Thorlabs

terometer described in Sec 3.1 and moved to a cleaner room at the DFA. The old setup, which was used to measure scattering in reflection, is illustrated in Fig. 3.9.

Similarly to the scatterometer, the laser in this setup had a wavelength of 1064 nm with a nominal power of 1W and a measured power of 1.1 W. The power sent into the system was controlled by a half-wave plate (indicated as $\lambda/2$ in the figure) and PBS system, where a quarter-wave plate ($\lambda/4$) was included to remove any ellipticity of the beam. A telescope (system of three lenses) was used to adjust the beam spot size on the sample, which was set to 707 μm. The beam then was reflected on two mirrors (M1 and M2) before reaching the sample at the back of the sphere. The specular reflection and the transmission were absorbed with dumpers to avoid extra contribution to the scattered light measurements and the transmission behind the first mirror was used to infer the incident power.

Measurements with the integrating sphere are made by using a reference measurement, which is made on a diffusive cap that can be attached to the opening of the sphere where the sample is usually placed, completely covering the opening. The diffusive cap is made of the same material as the inside of the sphere. We therefore assume that the TIS of the diffusive cap is equal to 1, so all TIS measurements made with the integrating sphere are normalized by the value measured with the diffusive cap.

The TIS is given by the ratio between the incident power and the scattered power (see Eq. 2.8). Since in real measurements there is always a background contribution, a single measurement is not enough to determine this. The relationship between the

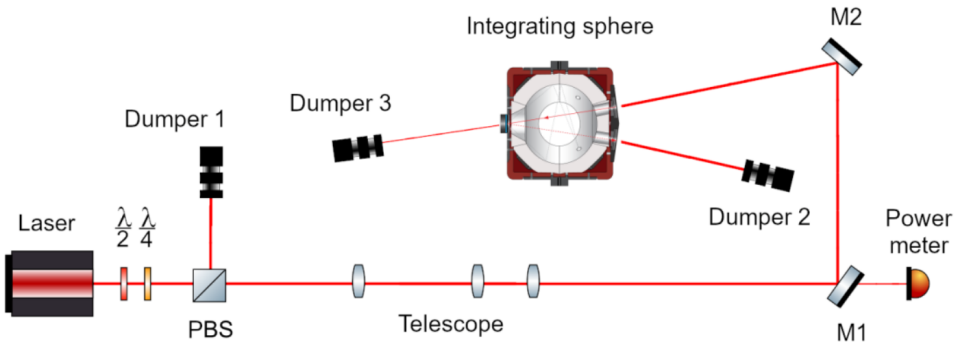

Figure 3.9: Old setup of the integrating sphere. Image credit: Leonardo Dal Cin

incident power and the scattered power is described by a straight line with slope m, translated vertically due to the background contribution B:

$$P_{in} = P_{scatt} * m + B, \tag{3.11}$$

where P_{in} is the incident power and P_{scatt} is the scattered power. The measurements must be made at various incident powers so that this line can be constructed and the slope m can be obtained. This is done for both the sample and the reference.

The background included in B is mostly due to the light in the laboratory or thermal radiation, which are constant and independent of the laser power. We also need to consider a background contribution due to scattering of the laser light on the air, which increases with the laser power. This is measured by considering that this contribution is the same as a measurement of a sample at infinity in the same conditions. To find the best approximation for this value we use a sample with very low TIS, like a dumper, and make various measurements of the slope m placing it at different distances from the opening of the sphere. The slope is expected to decrease until converging to the value at infinity, following an equation of the type:

$$m(d) = \frac{a}{(d-b)^2} + m_\infty, \tag{3.12}$$

where d is the distance between the dumper and the opening of the integrating sphere, a and b are fitting parameters and m_∞ is the value of the slope at infinity. By making a fit of the data with this function, we obtain the value for m_∞, which is subtracted from both the measurement of the sample and the measurement of the reference.

Finally, the TIS is obtained from

$$TIS = \frac{m_s - m_\infty}{m_{ref} - m_\infty}, \tag{3.13}$$

where m_s is the slope measured for the sample, m_{ref} is the slope measured for the reference, and m_∞ is the slope measured for the dumper at infinity, accounting for the air contribution.

3.2.1 Systematic Losses

When making measurements with the integrating sphere, we are subject to a few systematic losses when scattered light escapes from the inside of the sphere through the openings. This section presents an estimation of their magnitude to study their relevance to the TIS measurement.

One of the systematic losses is due to the openings where the incident beam enters the sphere and where the reflected beam emerges. These openings are centered at an angle of 8° from the surface's normal and have an aperture radius of $\theta_{rad} = 3°$ as seen from the sample. Let us call the fraction of light lost through these openings α.

Another way we can lose some scattered light from the sphere is through the spaces between the sample and the interior of the sphere. The light scattered by the sample goes through a conical-shaped port that reflects the light toward the inside of the sphere. However, around the opening where we position the sample, there is a small region on the inside of this port that is made of a different material from the inside of the instrument, as can be seen in Fig. 3.8. This "dead zone" may prevent a fraction of the scattered light from circulating inside the sphere. As a worst-case scenario, we consider that as if it were an empty space through which light is lost after being scattered from the sample. The width of the dead zone (distance between the sample and the diffusive material inside the sphere) is 3 mm.

The spacing between the sample and the interior of the sphere can also be increased due to the fact that some samples are placed on a holder that needs to be adjusted manually, so the surface of the sample is not completely aligned with the surface of the sphere. The total loss due to this spacing and due to the dead zone we call β. Fig. 3.10 illustrates the losses α and β.

The TIS calculated from Eq. 3.13 can be written as:

$$TIS = \frac{m_s - m_\infty}{m_{ref} - m_\infty} \approx \frac{TIS^*(1-\alpha_s)(1-\beta_s)}{TIS_{ref}(1-\alpha_{ref})}. \tag{3.14}$$

where the subscript s refers to the sample, ref refers to the reference (the diffusive cap) and TIS^* is the true TIS of the sample, corrected for the losses α and β. Here we neglected these losses for the air contribution. Since the TIS of the reference is defined as 1, we have:

$$TIS = \frac{TIS^*(1-\alpha_s)(1-\beta_s)}{1-\alpha_{ref}}. \tag{3.15}$$

The values of α_s and β_s can be estimated by making assumptions on the shape of the BSDF. We consider the case in which it follows the GHS model with typical fitting parameters, and the case in which it is a Lambertian emitter. Similarly, α_{ref} is estimated by considering Lambertian emission. The values are then estimated by integrating the BSDF in the regions of the openings and dividing by the integral of the BSDF over one hemisphere. The estimation of each of these losses is presented in more detail in the following.

Starting with the estimation of α_{ref}, we assume that the radiant intensity of the diffusive cap can be described by Lambert's law [7]:

$$I(\theta) = I_0 cos(\theta), \tag{3.16}$$

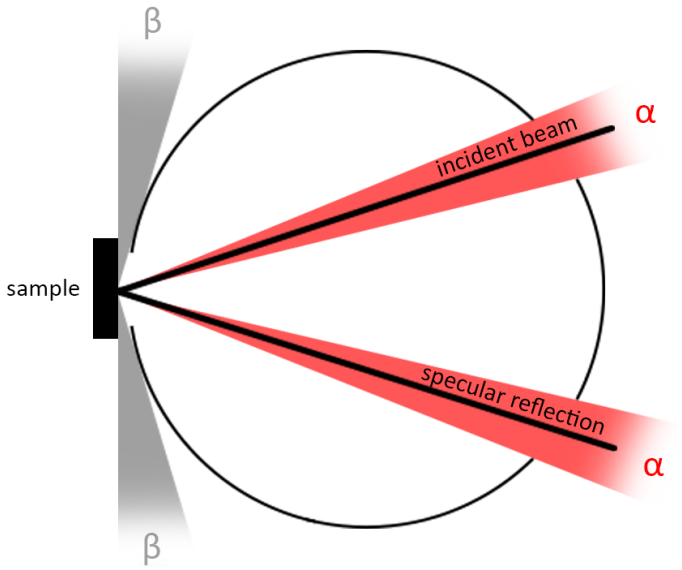

Figure 3.10: Losses in the integrating sphere due to the openings of the instrument. α is the loss due to the opening for the incoming beam and for the reflected beam, indicated in red. β is the loss due to the space between the sample and the sphere, indicated in grey.

where $I(\theta)$ is the radiant intensity, I_0 is the radiance of the material, which is the same as the BSDF of the diffusive cap, and θ is the angle from the surface's normal.

Since the BRDF of the diffusive cap is constant at all angles, the losses due to each of the openings for the incident beam and for specular reflection are equal to each other. The loss due to one of the openings is calculated as the ratio between the integral of Eq. 3.16 over the region where it falls inside the opening and the integral of the function over half a sphere. The total loss α is thus twice that value. We integrate in spherical coordinates and, for simplification, we approximate the circular area of the opening as a square with side $2\theta_{rad}$:

$$\alpha_{ref} = 2\frac{\int_{-3^\circ}^{3^\circ} d\phi \int_{8^\circ-3^\circ}^{8^\circ+3^\circ} \cos\theta\sin\theta d\theta}{\int_0^{2\pi} d\phi \int_0^{\pi/2} \cos\theta\sin\theta d\theta} \approx 0.1\% \tag{3.17}$$

This is also the α_s loss that we expect from a sample that behaves as a Lambertian emitter.

We now make the assumption that the BRDF of the sample follows the GHS model. Since the scattering function has a peak at angles near the specular reflection, the amount of light that is lost through the opening for the reflected beam is much greater than the amount that is lost through the opening for the incident beam, so we approximate the total loss as the loss due to the opening for specular reflection.

We calculate α_s as the integral of the BRDF over an angle of 3° around the

reflection peak divided by the integral of the BRDF over one hemisphere. To simplify the integral, we assume the BRDF to be spherically symmetric, and thus the out-of-plane BRDF becomes a rotation of the BRDF in the plane of incidence around its peak. For this, we use a translation of the function, making the peak centered at zero to perform the rotation:

$$BRDF(\theta_s + \theta_i, \theta_i) = b\left[1 + \left(\frac{\sin\theta_i - \sin(\theta_s + \theta_i)}{l}\right)^2\right]^{s/2} \tag{3.18}$$

The fitting parameters b, l and s can be found from a fit of data acquired with the scatterometer. The value of α_s is then calculated as

$$\alpha_s = \frac{\int_0^{\pi} d\phi \int_{-3^\circ}^{3^\circ} BRDF(\theta_s + \theta_i, \theta_i)\cos(\theta_s + \theta_i)\sin\theta_s d\theta_s}{\int_0^{2\pi}\int_0^{\pi/2} BRDF(\theta_s, \theta_i, \phi_s, \phi_i)\cos\theta_s\sin\theta_s d\theta_s d\phi_s}, \tag{3.19}$$

where the cosine term accounts for the change in the sample area viewed by the detector. Based on typical values of the fitting parameters obtained with the scatterometer (see Section 4.2), α_s is estimated to be about 3.5%.

To calculate β_s, we integrate the BRDF over the angle θ_x at which light can escape, as illustrated in Fig. 3.11. β_s is then the ratio between this value and the integral of the BRDF over an entire hemisphere:

$$\beta_s = \frac{\int_0^{2\pi}\int_{\pi/2-\theta_x}^{\pi/2} BSDF(\theta_s, \phi_s, \theta_i, \phi_i)\cos(\theta_s)\sin(\theta_s) d\theta_s d\phi_s}{\int_0^{2\pi}\int_0^{\pi/2} BSDF(\theta_s, \phi_s, \theta_i, \phi_i)\cos(\theta_s)\sin(\theta_s) d\theta_s d\phi_s}. \tag{3.20}$$

The angle θ_x can be calculated as $\arctan(h/r)$, where r is the radius of the opening of the integrating sphere where we place the sample, which is 13.5 mm, and d is the distance between the sample and the diffusive material in the sphere. For typical values of b, l and s, β_s is about 4.5% considering a distance d of 3 mm (the width of the dead zone).

In the case of a diffusive surface, the scattering is approximated by Lambert's law (Eq. 3.16), and the BRDF is the constant I_0. This gives:

$$\beta_s = \frac{\pi I_0 \sin^2(\theta_x)}{\pi I_0} = \sin^2(\theta_x). \tag{3.21}$$

For a distance d of 3 mm, this is $\approx 5\%$.

Following Eq. 3.14, for both the case in which the BRDF follows the GHS model and the case in which it is a Lambertian emitter, the total decrease in the measured TIS due to these losses is small ($< 8\%$), which indicates that in most cases it can probably be neglected. If it is of one's interest, these losses can still be calculated for a specific sample once the shape of the BRDF is known, following the procedure described above. It is worth noting that other losses were not considered, such as the light that is lost through the openings after multiple reflections inside the sphere, but they were assumed to be small and were therefore neglected.

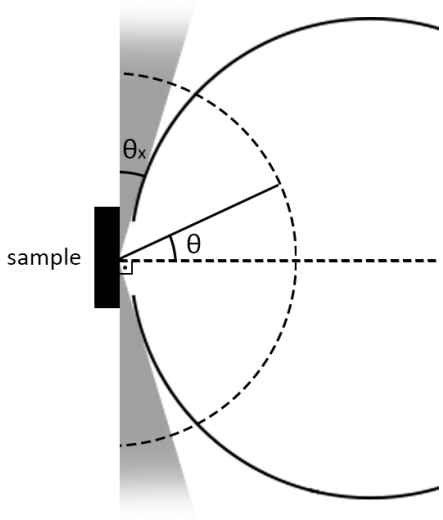

Figure 3.11: The coordinate θ and the angle θ_x indicated for a sample positioned by the opening of the integrating sphere.

3.3 Upgraded Setup

The scatterometer and the integrating sphere were combined in a new setup in the DFA, in Padova. The new version of the instruments is currently being built in a clean room, where we have fewer effects of scattering from dust on the surface of the sample, in the air, and in the optics. In this new setup both the scatterometer and sphere are hosted on the same bench and share the same laser sources, making it easier to obtain and compare multiple measurements of the same sample on those instruments. The new optical scheme is shown in Fig. 3.12.

The setup hosts 3 light sources, lasing at different wavelengths: in addition to the one at 1064 nm used in the previous setup, corresponding to the wavelength used in AdVirgo and other advanced detectors, we have a candidate wavelength for the ET, 1550 nm, and a shorter wavelength in the green, at 532 nm. The shorter wavelength is used as an auxiliary laser in AdVirgo and can also be used to understand what kinds of particles are responsible for the observed scattering. In the future, another candidate wavelength for the ET will be included, at 2000 nm.

For each of the lasers, there is a system of a HWP and PBS to control the power. In this setup, the HWP is motorized (indicated as MHWP in the figure) so that it can later be controlled from a computer, allowing us to match better the scattered light reaching the photodiode with its dynamic range and saturation level. After the PBS, there is another HWP, to be controlled manually, to change the direction of polarization of the light beam we send to the samples under study.

The laser beam is sent to either the scatterometer or the integrating sphere by making use of flip mirrors (indicated as "FM" in the figure). The flip mount allows the mirror to be oriented in two positions orthogonal to each other so that it either

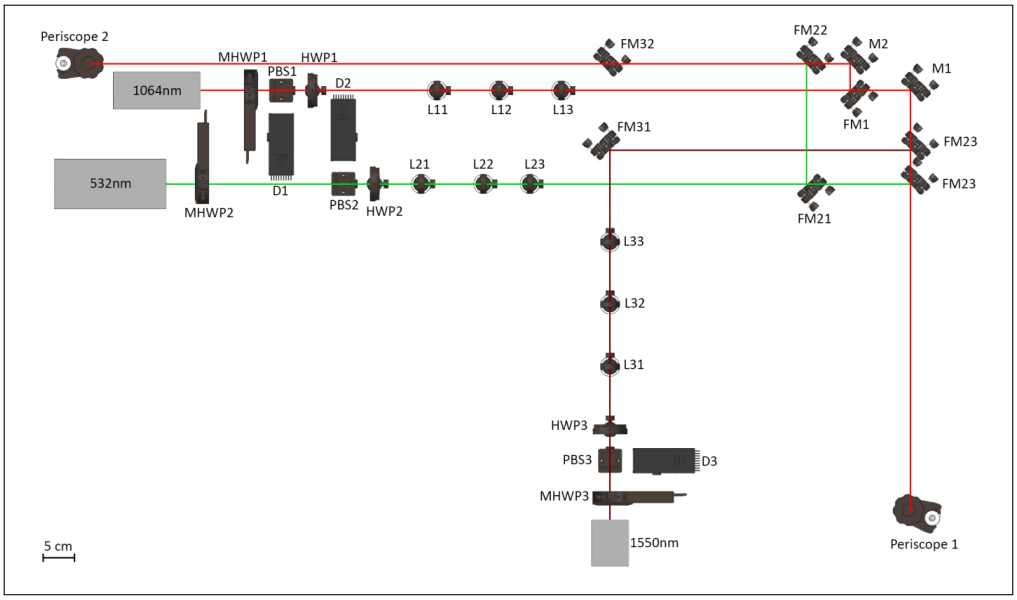

(a) First level.

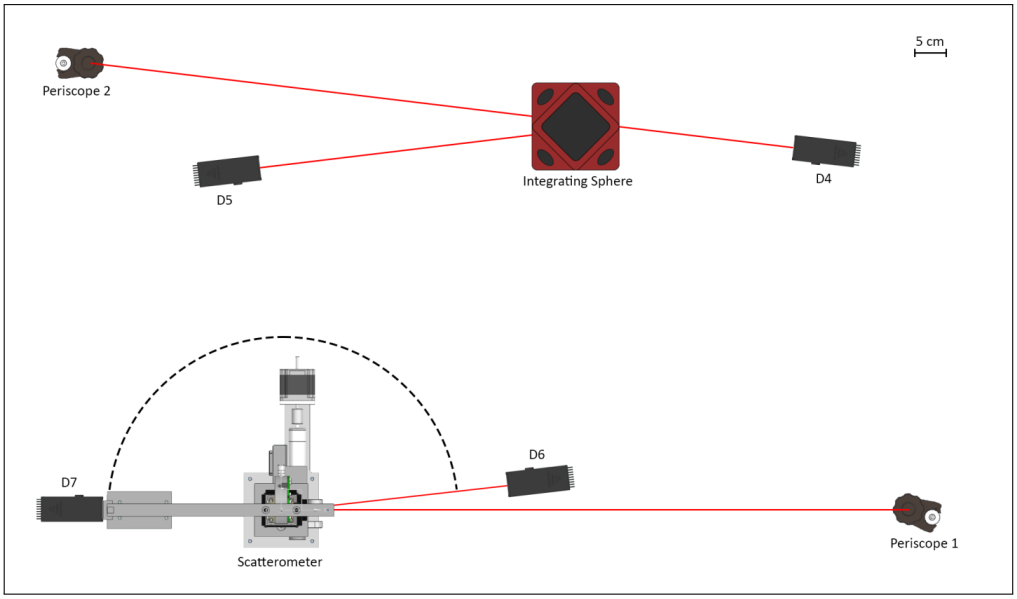

(b) Second level.

Figure 3.12: New setup of the instrument

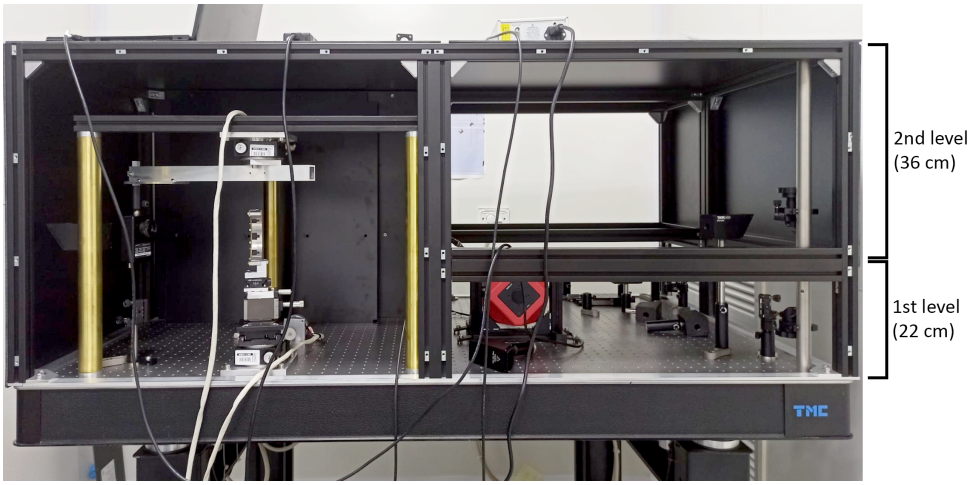

Figure 3.13: Upgraded setup of the scatterometer in the process of being mounted. The two levels are indicated with respective heights and the scatterometer can be seen on the left, occupying both levels.

intercepts or not the laser beam. The new version of the instrument is enclosed by a plastic black box that shields it from environmental light and dust. Internal panels of the same plastic allow to separate different parts of the experimental setup. This develops in two levels from the bench surface: the first level is where most of the optics are placed, while the second level contains the integrating sphere. The structure of the scatterometer occupies both levels, with the sample at the height of the second level. Fig 3.13 shows a picture of the scatterometer and the 2-level structure in the process of being mounted.

Each of the laser lines passes through a telescope consisting of a system of 3 lenses, that will allow us to change the beam spot size on the sample. By using a small spot size, we see how small imperfections on the surface of the sample affect the BSDF. By using a big spot size, we measure a BSDF averaged over a larger area, making the contribution of single imperfections less important.

Finally, the laser light is sent from the first to the second level through periscopes, which consist of two mirrors placed on a vertical structure. Depending on the positions of the flip mirrors, the laser beam will be sent to Periscope 1 or Periscope 2 and reach either the integrating sphere or the scatterometer.

The previous version of the scatterometer was limited by the size of the detector when making measurements close to specular reflection. To avoid scattering of the beam off the surface of the detector, the minimum angle at which measurements were made was 13 degrees from specular reflection. The upgraded version of the scatterometer has a new arm that will allow us to make measurements closer to specular reflection. Instead of placing the detector directly facing the sample, it will be placed horizontally on top of the arm, and there will be a small prism reflecting the scattered light toward it. This is illustrated in Fig. 3.14. The lateral size of the prism is about 3 mm, which allows for a minimum measurement angle of ≈ 0.3 degrees from specular reflection.

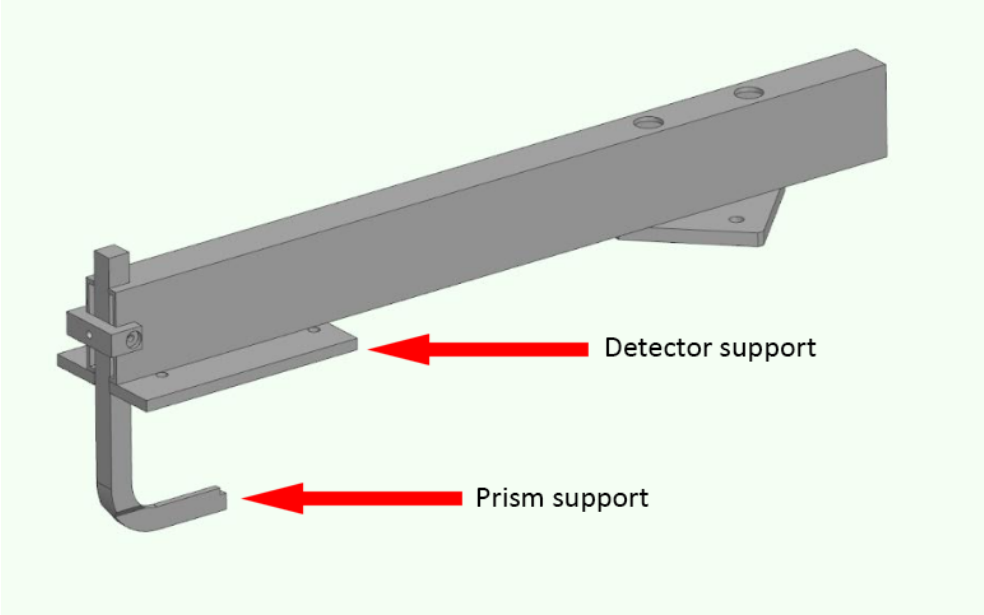

Figure 3.14: Arm that supports the detector of the scatterometer in the new setup. The detector will be positioned facing downwards and a prism will direct the signal to the detector.

Similar to the old versions of the instruments, the specular reflection and the transmission are absorbed by dumpers to avoid unwanted reflections creating noise.

3.4 Beam Propagation

Since we work with lasers in the instrument, it is important to study how they propagate through the different optics, accounting for the spot size of the beam on the different components to avoid unwanted scattering. Moreover, we make use of telescopes to control the beam spot size on the sample and study how the scattering is affected by small surface imperfections.

3.4.1 Gaussian Beams

When working with the lasers we are dealing with Gaussian beams. Gaussian beams have a characteristic intensity profile that makes them easily predictable at a given distance. They have this name because, when looking at the transversal profile of the beam, the irradiance as a function of the distance x from the center of the beam has a Gaussian shape:

$$f(x) = a \exp\left(-\frac{x^2}{2\sigma^2}\right), \tag{3.22}$$

with a the central amplitude and σ the standard deviation. This is illustrated in Fig.3.15. The distance at which the irradiance is a factor $1/e^2$ smaller than the

maximum irradiance is called the beam radius, and is equal to 2σ. It is described by the equation [2]

$$w(z) = w_0 \sqrt{1 + \left(\frac{(z - z_0)\lambda}{\pi n w_0^2} \right)^2}, \tag{3.23}$$

where $w(z)$ is the radius as a function of the position z on an axis aligned with the direction of propagation of the beam. w_0 is called the "waist" of the beam: it is the smallest value of the radius, located at position z_0. This evolution of $w(z)$ also depends on the wavelength λ and the index of refraction of the medium.

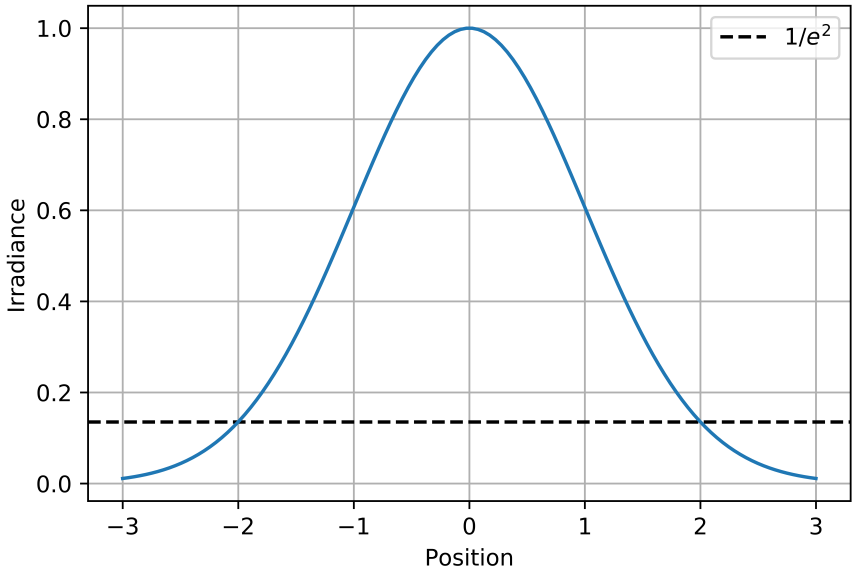

Figure 3.15: Example of transversal profile of a Gaussian beam in arbitrary units. On the horizontal axis, the position with respect to the center of the beam is indicated. Here, $\sigma = 1$ and $w = 2$.

3.4.1.1 Thin Lens

In a thin lens, the thickness of the lens is much smaller than the radius of curvature of its surface. When building the telescopes for the new instrument, we make use of lenses that can be approximated as thin lenses for the purpose of predicting the behavior of the beam.

As light from an object goes through a lens, an image of the object is formed by the lens with a different size from the original object and at a different distance from the lens. In geometric optics, we can use the well-known thin-lens equation:

$$\frac{1}{s} + \frac{1}{s'} = \frac{1}{f}, \tag{3.24}$$

where s and s' are the distances from the object to the lens and from the image to the lens, respectively, and f is the focal length of the lens.

When we consider a Gaussian beam, the equation from geometric optics needs to be modified to account for the beam's properties in physical optics. Eq. 3.24 then becomes [24]:

$$\frac{1}{s + {z_R}^2/(s-f)} + \frac{1}{s'} = \frac{1}{f}, \tag{3.25}$$

where z_R is the Rayleigh range of the beam before the lens, equal to $\pi w_0^2 n/\lambda$, with n the index of refraction of the medium and λ the wavelength of the light beam. Considering the beam waist as an object with size w_0, the magnification is

$$\frac{w_0'}{w_0} = \frac{f}{\sqrt{(s-f)^2 + {z_R}^2}}. \tag{3.26}$$

Rearranging Eq. 3.25 and Eq. 3.26, we have expressions for ${w_0}'$ and s' as a function of the other parameters:

$$s' = \frac{-f\left(s + \frac{{z_R}^2}{(s-f)}\right)}{f - \left(s - \frac{{z_R}^2}{(s-f)}\right)}, \tag{3.27}$$

$$w_0' = w_0 \frac{f}{\sqrt{(s-f)^2 + {z_R}^2}} \tag{3.28}$$

3.4.2 Laser Characterization

To properly design the optical setup it is important to characterize the mode of the laser sources, i.e. the waist size and position of the beam emitted by the device. The lasers at 532 nm and 1550 nm to be used in the setup were already used and characterized in the past [15][16]. The one at 1064 nm has been characterized in the context of this thesis work.

The laser at 532 nm was characterized by using a beam profiler to measure the radius along the beam. The following waist value and position were found in the x and y directions (corresponding to the horizontal and vertical positions in the plane transverse to propagation):

	x	y	average
w_0	$(49 \pm 2)\mu$m	$(44 \pm 2)\mu$m	$(46 \pm 1)\mu$m
z_0	(-18 ± 4) cm	(-13 ± 4) cm	(-16 ± 3) cm

For simplification, we used the average value for the telescope simulations. z_0 was measured from a point 20 cm in front of the laser output, so the average corresponds to (4 ± 3) cm from the output.

For the laser at 1550 nm, the knife-edge test was used at two different positions z from the laser output, to measure $w(z)$. The results are shown in Table 3.1.

z	$w(z)$
50 cm	$(808 \pm 5)\mu$m
120 cm	$(997 \pm 7)\mu$m

Table 3.1: Beam radius $w(z)$ at different positions z for the laser at 1550 nm.

With this, we can use approximate the beam parameters as $w_0 = 785\mu$m and $z_0 = 0.22$ m, which satisfy the values in Table 3.1.

The laser at 1064 nm was characterized by measuring the beam radius at various points along the direction of propagation using a beam profiler. At each position, 10 subsequent measurements of the radius were made and the average was taken. The result was fitted with Eq. 3.23, as shown in Fig. 3.16. The resulting values are shown in Table 3.2.

	x	y	average
w_0	$(365 \pm 5)\mu$m	$(359 \pm 5)\mu$m	$(362 \pm 3)\mu$m
z_0	(23.3 ± 0.8) cm	(20.4 ± 0.8) cm	(22 ± 0.7) cm

Table 3.2: Beam waist w_0 and respective position z_0 for the laser at 1064 nm, along the x and y directions.

3.4.3 Designing the Telescopes

For controlling the beam spot size on the sample, we make use of a telescope for each laser. The telescope consists of a system of 3 lenses in which one is moved to change the spot size. The choice of the focal length and position of each lens, as well as which lens should be movable in the setup was made based on simulations. We note that, excluding cases of extreme divergence, we are generally only interested in the spot size on the sample, and not in the position of the waist. On the other hand, in designing the beamline it is important to check that the beam never becomes so big that clipping on the optical elements becomes a concern.

The first step in the simulation was making use of the software JamMT [30]. It simulates the behavior of a Gaussian beam as it goes through different lenses. It also contains a mode matching tool, which finds all possible solutions for obtaining the resulting beam of our choice, given all available lenses, the number of lenses to be used, and the range in which they can be placed, among other settings.

After using the mode matching tool to find possible solutions, we used a Python script that, just like JamMT, simulates the behavior of the beam given the lenses and respective positions. Unlike JamMT, this script does not provide telescope solutions, but, given the set of lenses, it simulates the behavior of the output as a lens is moved. To estimate the resulting spot size, it uses Eq. 3.27 and 3.28. Applying this to each

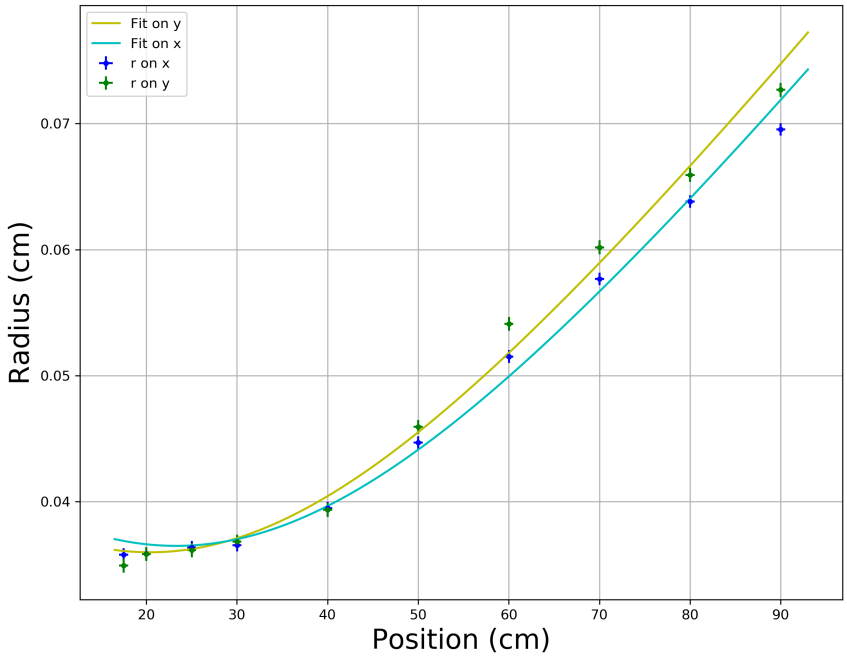

Figure 3.16: Propagation of laser at 1064 nm. The radius was measured with a beam profiler and fitted with the Gaussian beam equation. The position was measured from the laser output.

of the 3 lenses, we find the final value of the waist and its position after the third lens. Inputting these values into Eq. 3.23, we can calculate the value of the beam radius at any distance from the laser output.

The script then simulates the resulting beam after moving each of the lenses in small steps. While one lens is moved, the other two stay in the original position. The simulation was programmed to move the first and third lenses 10 cm to the left and 10 cm to the right. This movement is stopped if they become too close to the second lens, in case the distance between them is less than 10 cm. We set this limit at a 2 cm distance from the other lens. The middle lens is moved in the entire range between the first and third lenses, respecting the 2 cm limit.

By moving one of the lenses, both the waist size and its position change. We thus started by finding solutions with JamMT where the smallest desirable spot size is the waist and is at the distance of the sample. When a lens is moved, the waist position moves away from the sample, increasing the spot size. The choice of 3 lenses was due to the fact that, with 2 lenses, either there were no solutions found by JamMT or the simulation shows that the system was extremely sensitive, i.e., moving the lens by a few millimeters changed the spot size by hundreds of micrometers, making it difficult

to reach the desired result with good precision.

Another factor that needed to be considered was the divergence of the beam, which increases as the waist size decreases. Since the distance between the sample and the dumpers that absorb the specular reflection and transmission is considerably large (about 40 cm), if the spot size is small on the sample, it could mean that it is too big on the dumpers, causing clipping of the beam and generating background noise from stray light. This is also a concern for the optics in the instrument. We thus simulated the beam spot size not only on the sample but also on each of the mirrors and on the third lens of the telescope, where the beam had the biggest radius due to the large distance from the waist.

The clipping is the fraction of light falling outside of the aperture of the optics. This increases if the beam is not centered with the aperture. We considered a maximum distance between the center of the beam and the center of the aperture of 2 mm as a worst-case scenario in alignment error and aimed at having clipping below 10^{-6} at all times, which is the limit used in AdVirgo.

The plots generated with the Python script included the beam spot size on the various optics and on the sample as a function of the position of the movable lens of the telescope. This was made for various solutions presented by JamMT. The distance from the laser output to the sample on the integrating sphere and on the scatterometer is similar (differing by a few centimeters and not precisely defined in the initial design), so we used an approximated distance to calculate the radius on the sample for both instruments.

The criteria for choosing the best solution for the setup were a few. First, we needed to have a large spot size range on the sample, meaning from about 250 μm to 1500 μm. We then took into account the sensitivity of the system, giving preference to the systems in which this change happened slower as we move the lens so that we can more easily set the desired spot size. Finally, in all positions where the lens is placed, the clipping on all optics and on the dumper should be below the set limit.

3.4.3.1 Laser at 1064 nm

For the laser at 1064 nm, the chosen setup is shown in Table 3.3. The third lens is used to control the spot size, so it was placed on a linear translator. Fig. 3.17 shows the simulation of the beam spot size on the different optics, on the dumpers, and on the sample as a function of the position of the third lens. The maximum radius allowed on the optics and on the dumpers to stay below the clipping limit is also indicated.

	Lens 1	Lens 2	Lens 3
Focal distance (mm)	50	150	300
Position (m)	0.64	0.73	1.03

Table 3.3: Telescope for laser at 1064 nm. The position is measured from the laser output and Lens 3 is moved to control the spot size.

The standard size of the optics used in the instrument is 1", but using bigger ones if necessary to avoid clipping was considered. From Fig. 3.17 we see that using optics

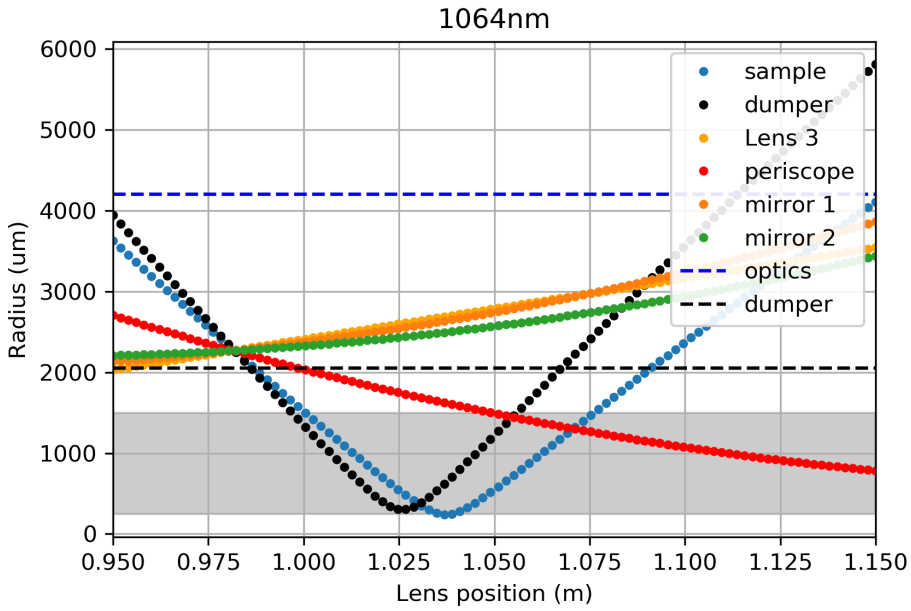

Figure 3.17: Simulation of the beam radius for the laser at 1064 nm on the different components of the instrument and on the sample. The blue horizontal line and the black horizontal line show the limit under which we have an amount of clipping below 10^{-6} for optics with a diameter of 1" and for the dumpers, respectively. The range of interest for the radius on the sample is highlighted in grey.

Lens 3 position (mm)	w_0 (μm)	z_0 (cm)
0	188 ± 1	262.9 ± 0.3
15	234 ± 3	291.3 ± 0.7
27	296 ± 5	326 ± 1
35	350 ± 5	360 ± 2
50	518 ± 20	462 ± 7

Table 3.4: 1064 nm laser characterization for different positions of the third lens on the linear translator.

of 1" is enough to stay below the imposed clipping limit since the radius on all optics is below the blue line for all positions of the movable lens.

Using a beam profiler, we characterized the laser beam for a few different positions of the movable lens. Measured on the micrometer of the linear translator, these positions are 0 mm, 15 mm, 27 mm, 35 mm, and 50 mm. When the micrometer measures 0 mm, the lens is the farthest away from the laser output, at a distance of 0.99 m, getting closer as we move toward 50mm. For each position of the lens, the beam radius $w(z)$ was measured at 7 different distances z from the laser output and, at each z, 10 subsequent measurements were made and the average was taken. The plot of the average $w(z)$ versus z was fitted with Eq. 3.23 for each position of the lens and the values of w_0 and z_0 were found. The results can be found in Table 3.4.

Based on these measurements, the value of the radius at a distance of 3 m from the laser output was calculated with Eq. 3.23 for each lens position. This is approximately the distance at which the sample will be located. The result is shown in Fig. 3.18. The behavior of the spot size follows the shape expected from the simulation. With this, we obtain a minimum spot size on the sample of 265 μm, when the lens is at 15 mm, and a maximum spot size of 1181 μm, when the lens is at 50 mm.

It is worth mentioning that the lenses used in the setup are manufactured for a wavelength of 532 nm, while JamMT and the Python simulation considered lenses for 1064 nm. The focal distance of real the lenses is therefore slightly different (about 12%) from the nominal ones in Table 3.3, which could cause small deviations from the predicted behavior of the telescope. This is also the case for the laser at 1550 nm.

3.4.3.2 Lasers at 532 nm and 1550 nm

The telescopes for the lasers at 532 nm and 1550 nm were not mounted as part of this thesis, but the simulations were made and the telescope solutions were chosen.

The solution for the laser at 532 nm can be found in Table 3.5 and the simulation showing the beam spot size on the different components in Fig. 3.19. For this telescope, we are well below the imposed clipping limit even with optics of 1".

The solution for the laser at 1550 nm can be found in Table 3.6. Fig. 3.20 shows the simulation of the beam spot size. Due to the longer wavelength, this laser has a bigger divergence and we are slightly above the clipping limit of 10^{-6} on the dumper

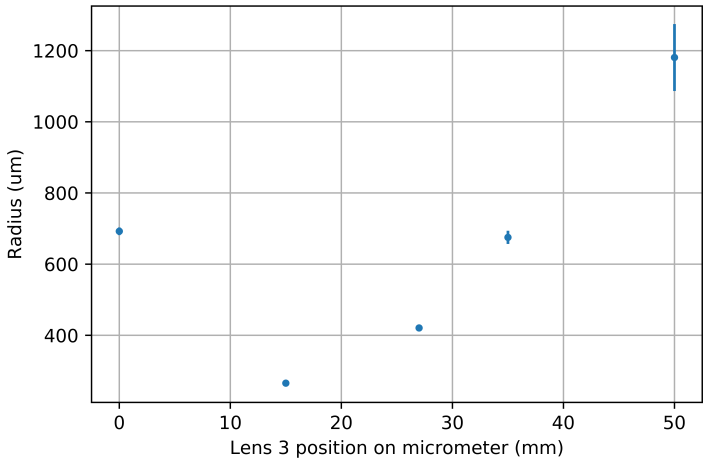

Figure 3.18: Spot size of laser at 1064 nm at a distance of 3 m from the output, estimated based on measurements of w_0 and z_0 for different positions of the movable lens in the telescope.

	Lens 1	Lens 2	Lens 3
Focal distance (mm)	50	125	300
Position (m)	0.22	0.35	0.57

Table 3.5: Telescope for laser at 532 nm. The position is measured from the laser output and Lens 3 is moved to control the spot size.

when the spot size on the sample is at the desired maximum of 1500 μm. This limit, however, was calculated considering a displacement of the laser beam of 2 mm from the center of the aperture. This value is a worst-case scenario accounting for a possible error made by eye when positioning the sample, and it is likely to be much smaller on the dumper due to its smaller aperture which can be used as a guide when aligning the beam. Reducing this displacement to 1.5 mm, the clipping decreases by about an order of magnitude for the same spot size, so it is unlikely that the clipping on the dumper would be problematic.

4 Measurements

In order to study the performance of the instruments used to measure the scattering and test the measurement procedures, a few measurements were made. This was done by measuring various samples with different properties, comparing repeated measurements of the same sample, and comparing measurements made with the two instruments. The GHS model was also tested by using it to fit the scatterometer data

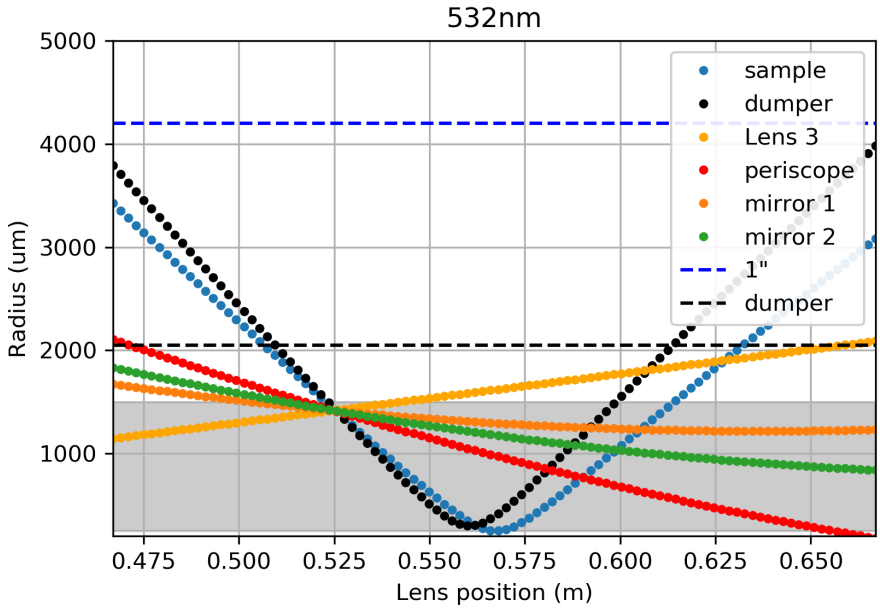

Figure 3.19: Simulation of the beam radius on the different components of the instrument and on the sample. The blue horizontal line and the black horizontal line show the limit under which we have an amount of clipping below 10^{-6} for optics with a diameter of 1" and for the dumpers, respectively. The range of interest for the radius on the sample is highlighted in grey.

and obtain the TIS, which was compared with the TIS measured with the integrating sphere.

The measurements were made with the original setups of the scatterometer and the integrating sphere, before they were combined into a single setup and brought to a clean room. With this, we also estimated the background contribution in each of the laboratories where the instruments were located, which we can consider to be an upper limit on the background we expect to have in the clean room.

4.1 Repeatability of Sample Mounting

The sample in the scatterometer is placed on a holder, where it is secured with screws that lightly press against it (See Fig. 3.2). Since this procedure of mounting the sample is done manually and leads to small changes in position with each mount, we wanted to investigate how much a measurement can change due to remounting the sample. The procedure was done with the old setup of the scatterometer, not yet in a clean room. Although dust can affect the results by creating some deviation in the BSDF, the measurements are still useful to establish an upper limit on the amount of variation we expect between mounts.

The repeatability of the sample mounting procedure was studied with a double-

	Lens 1	Lens 2	Lens 3
Focal distance (mm)	50	50	200
Position (m)	0.23	0.26	0.49

Table 3.6: Telescope for laser at 1550 nm. The position is measured from the laser output and Lens 1 is moved to control the spot size.

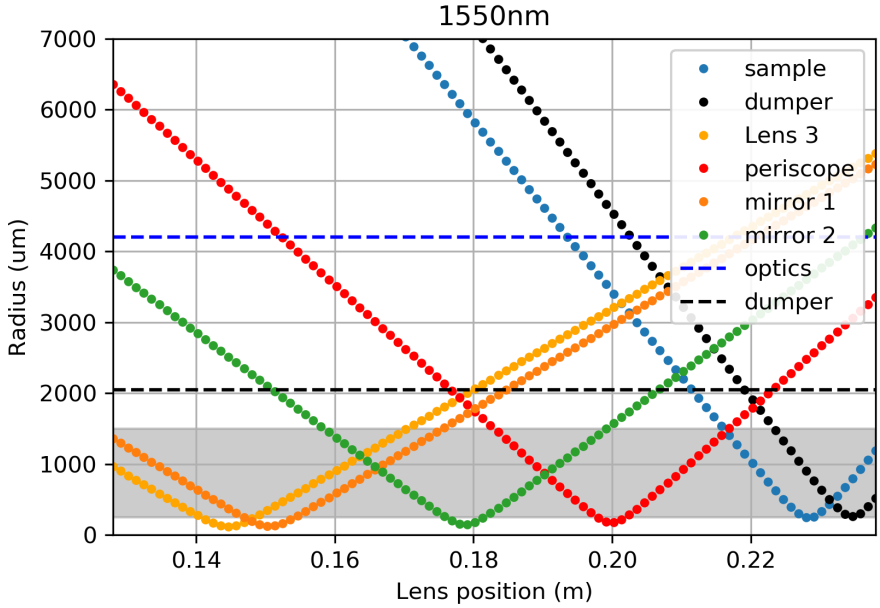

Figure 3.20: Simulation of the beam radius for the laser at 1550 nm on the different components of the instrument and on the sample. The blue horizontal line and the black horizontal line show the limit under which we have an amount of clipping below 10^{-6} for optics with a diameter of 1" and for the dumpers, respectively. The range of interest for the radius on the sample is highlighted in grey.

side polished silicon sample. We used a sample with a large surface area, about 15x15 cm, to avoid possible scattering of the laser light off the edges of the sample. A big sample also allowed us to make measurements on different zones of the sample's surface to study how the BSDF changes according to the part of the sample on which we measure. The holder can be horizontally translated with a micrometer, so this was used to set three different positions (each 5 mm apart) on the sample where measurements were performed.

For each of the three positions, four measurements were made. Between each measurement, both the sample and the sample holder were removed and placed back in position. All measurements were performed with the same laser power. Fig. 4.1 shows the measurements for each position.

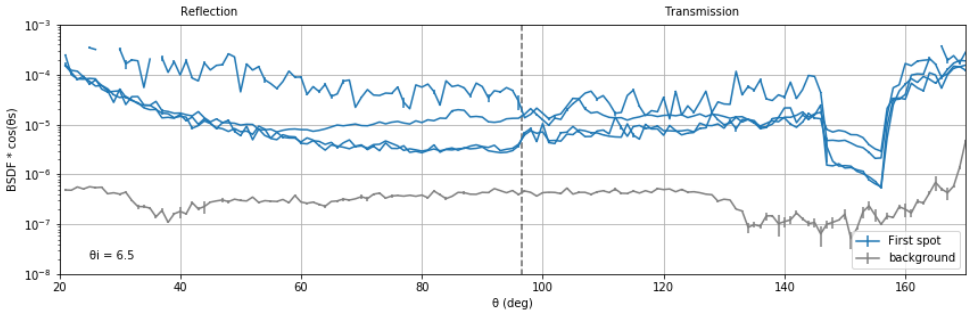

(a) First position.

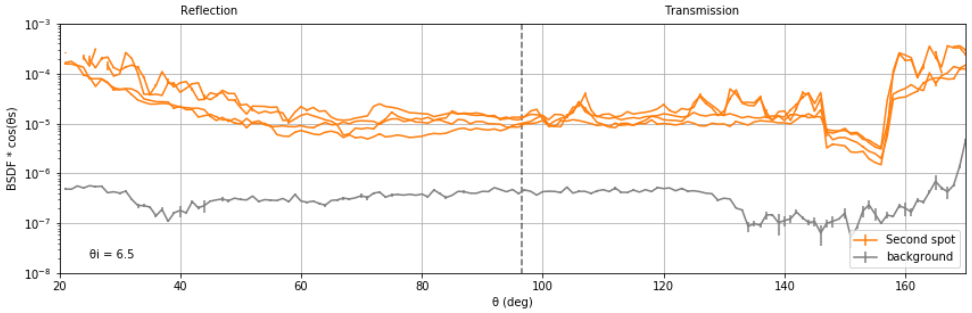

(b) Second position.

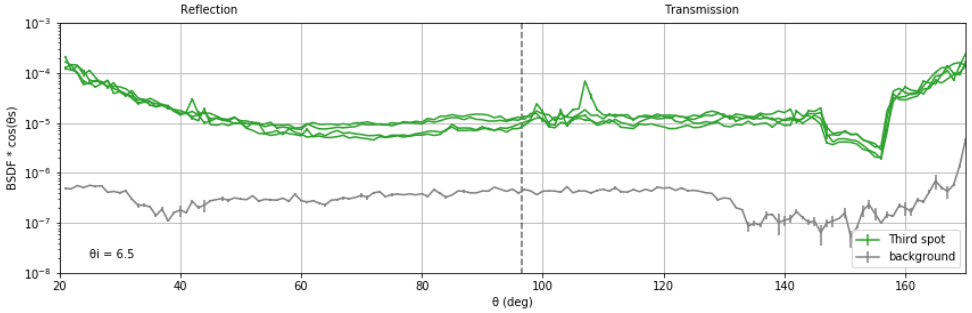

(c) Third position.

Figure 4.1: Repeated measurements on three different positions on silicon sample.

The results display a low level of variability for the same position; however, some measurements have an unusually high level of scatter with respect to the others. One of the measurements of the first position is about an order of magnitude higher than other measurements at most angles, while another one seems to deviate from the others between $\theta \approx 60°$ and $\theta \approx 130°$. The measurements of the second position seem to follow two different curves, especially at $\theta < 60°$ and $\theta > 120°$, about half an order of magnitude apart. This is also the case for a small part of the BSDF of the third position, between $\theta \approx 60°$ and the transition into transmission.

We did not find any correlation between neither the order in which measurements were taken, the position of measurement, or the mount run with the scattering level. The large variations in the BSDF between each mount could be due to dust or scratches on the surface that were hit with a small displacement of the sample. Performing this same procedure with the new setup and different samples might give a better understanding of the cause of this deviation.

4.2 Baffle Samples

The measurements by the integrating sphere and by the scatterometer were compared for the first time using samples of materials used on the stray-light baffles in the Virgo interferometer. These measurements allowed us to test the instruments and modeling methods by comparing the value of the TIS calculated from integrating the BSDF, acquired with the scatterometer, and the TIS measured directly with the integrating sphere. Measurements of the TIS of these samples were previously performed at EGO (European Gravitational Observatory, the institution that manages and hosts Virgo) with an integrating sphere, with which we compared our results.

We used four stainless steel samples provided by *Optimask* (Paris), which deposited a Cr/Cr_2O_3 2-layer anti-reflective coating on them. They came in two pairs, which were identified as '68B' and '69B'. For each pair, one sample seemed to have the same texture on its entire surface, so we called these "uniform". The other piece in the pair had a stripe with a different texture on the bottom, as illustrated in Fig. 4.2, which we called "non-uniform".

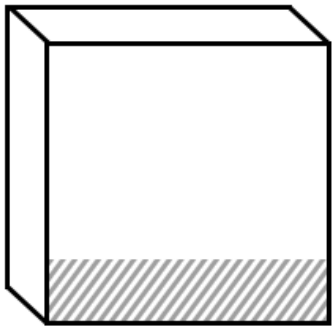

Figure 4.2: Illustration of non-uniform baffle sample, with the stripe of different texture indicated in grey.

4.2.1 BSDF and TIS via Scatterometer

We performed measurements of the BRDF of the baffle samples in the incidence plane at an incidence angle of $\theta_i = 6.5°$, which is the minimum possible angle considering the size of the dumper that absorbs the specular reflection. Since we did not expect any transmitted radiation and were interested only in the BRDF for the TIS estimation, we limited ourselves to measure from $\theta_s = 0°$ to $\theta_s = 90°$. In practice, the minimum angle at which data was acquired was $\theta_s = 13.5°$ from the normal of the sample, since we had to avoid going over the specular reflection with the detector. We only considered data up to an angle $\theta = 85°$, since at around that angle we have an abrupt decrease in the BSDF as the detector aligns with the plane of the surface.

For each of the samples, we performed 3 measurements corresponding to a different horizontal position on the sample's surface. The resulting BSDFs are shown in Fig. 4.3. As expected, the BRDF increases the closer to the angle of specular reflection. We notice that the non-uniform samples present slightly higher scattering on average in comparison to the uniform samples.

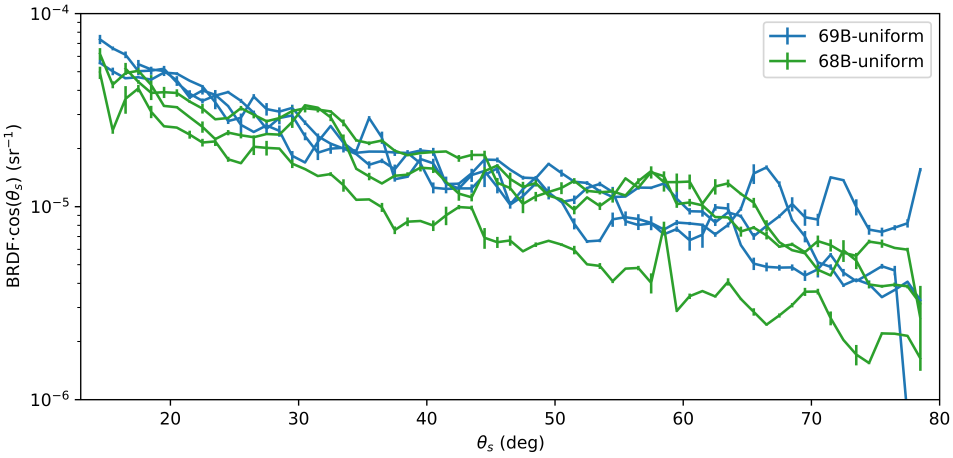

(a) Uniform samples.

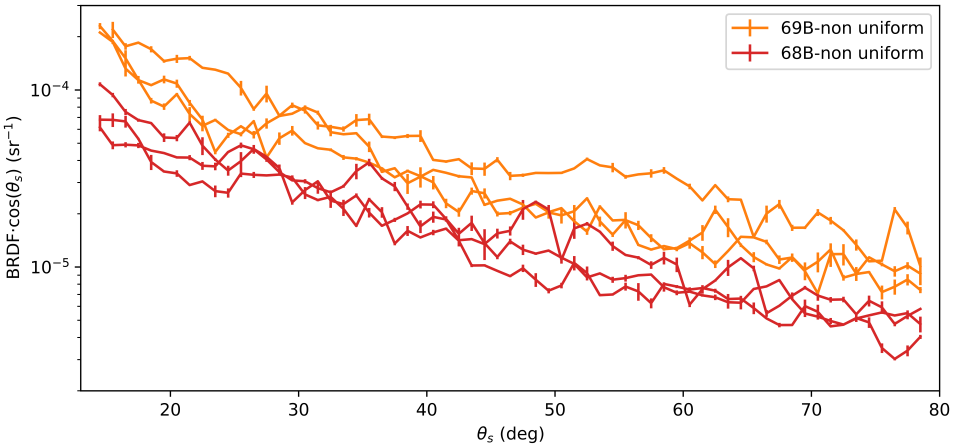

(b) Non-uniform samples.

Figure 4.3: BRDF measured on the 4 samples as a function of the angle θ_s from the surface's normal.

The BRDF data acquired with the scatterometer was fitted with the GHS model in the plane of incidence (Eq. 2.23), approximated for smooth surfaces. As a first test of the procedure, we took the average of the 3 measurements of each sample and we used this to estimate the corresponding GHS function parameters b, l, and s. The fits performed are shown in Fig. 4.4a as dashed lines. Fig. 4.4b shows the fit in more detail for the region where we have the data. We notice that at large angles the data has a slight increase with respect to the model, which could be due to some background effect, dust, the cosine term when converting the power to BSDF (Eq.3.1), or some other effect that we have not yet explored. Since this increase is small, we kept this data when making the fit. The resulting fitting parameters for each sample are listed in Table 4.1.

We notice that the parameters b and l have very large errors. This can likely be attributed to the fact that we do not have data near the specular reflection, which would give a better estimation of these parameters. The new version of the scatterometer should greatly reduce this problem since the new design of the arm allows for measurements closer to specular reflection.

	69B uniform	69B non-uniform	68B uniform	68B non-uniform
b (sr^{-1})	0.004 ± 20	0.08 ± 1000	0.004 ± 70	0.0000002 ± 0.7
l	-0.0006 ± 5	-0.0004 ± 7	$-.0003 \pm 10$	-0.002 ± 0.8
s (10^{-2})	-70 ± 6	-100 ± 7	-70 ± 6	-87 ± 5

Table 4.1: Fitting parameters for BSDF using GHS model on data from baffle samples.

The TIS was calculated from the BSDF by inserting the fitting parameters b, l, and s into the out-of-plane model (Eq. 2.19), and integrating over an entire hemisphere. The results are shown in Table 4.2. Errors were calculated with the bootstrap method and taking the 95% confidence interval. This is illustrated in Fig. 4.5 for the sample "68B non-uniform". We notice that a big variation in the peak due to the large errors in the b and l parameters does not result in big changes in the value of the TIS. In fact, by integrating the out-of-plane fits only in the region of the peak that is missing from the data, we find that this represents a maximum of 12% of the entire TIS.

Sample	69B uniform	69B non-uniform	68B uniform	68B non-uniform
TIS from BSDF (ppm)	75^{+6}_{-4}	175^{+13}_{-11}	63^{+3}_{-4}	78^{+4}_{-8}

Table 4.2: TIS estimated from a fit of data acquired with the scatterometer.

To ensure that the increasing data at large angles was not affecting the result significantly, this procedure was repeated including only the data until 60°. This increases the final estimated TIS, but the results do not present great changes, with a maximum increase of 13% for the sample "69B uniform", and less than 5% for the other samples.

This procedure was repeated for the individual measurements of the same sample, without averaging the BSDF of the three spots. The final TIS values are presented

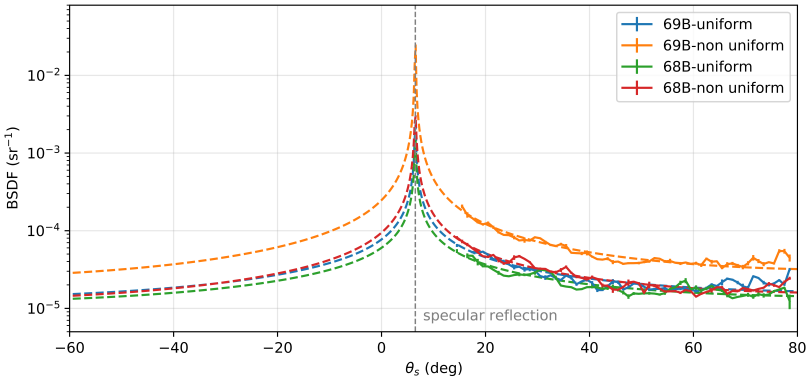

(a) Complete model.

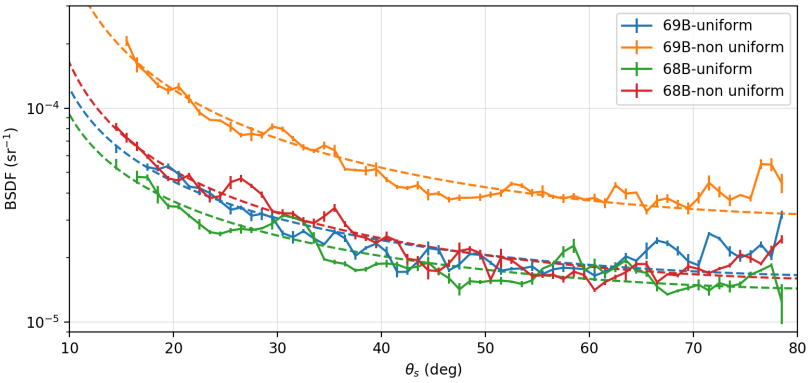

(b) Model in the region where we have the data.

Figure 4.4: GHS modeling of average BSDF for the 4 samples.

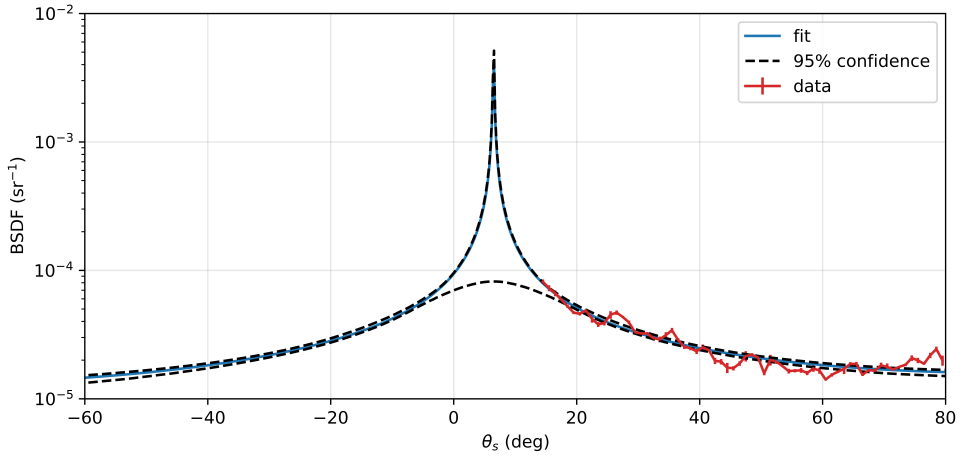

Figure 4.5: 95% confidence interval calculated with the bootstrap method for the average BSDF measured for the sample "68B non-uniform". The fit of the data is shown in blue.

Sample	69B Uniform	69B Non-uniform	68B Uniform	68B Non-uniform
Measurements	70^{+10}_{-7}	150^{+20}_{-30}	38^{+7}_{-4}	65^{+6}_{-9}
(ppm)	83^{+9}_{-8}	230^{+10}_{-20}	70^{+6}_{-6}	82^{+7}_{-7}
	66^{+6}_{-4}	140^{+20}_{-30}	77^{+7}_{-5}	84^{+5}_{-12}
Mean± MR	73 ± 9	170 ± 40	61 ± 20	77 ± 9

Table 4.3: TIS estimation from integrating the BSDF measured on different points of the 4 baffle samples. The mean and midrange (MR) for each sample are indicated.

in Table 4.3 and shown in Fig. 4.6. Generally, the spread of the measurements for the same sample is of the same order of the error associated with each measurement, making it difficult to draw conclusions about the uniformity of the scattering across the surface. However, we notice a bigger spread in the values corresponding to the sample 69B non-uniform with respect to the others, as well as higher values of the TIS. The sample 68B-uniform seems to be less homogeneous than the corresponding non-uniform sample, as can already be noted from the BRDF data.

4.2.2 TIS via Integrating Sphere

The measurement of the TIS made with the integrating sphere was done by measuring the slope of proportionality between the photocurrent generated by the scattered power as measured by the instrument's detector versus the incident power inferred by a powermeter placed behind the first mirror of the setup. All the measurements presented in this section were performed over the span of two days.

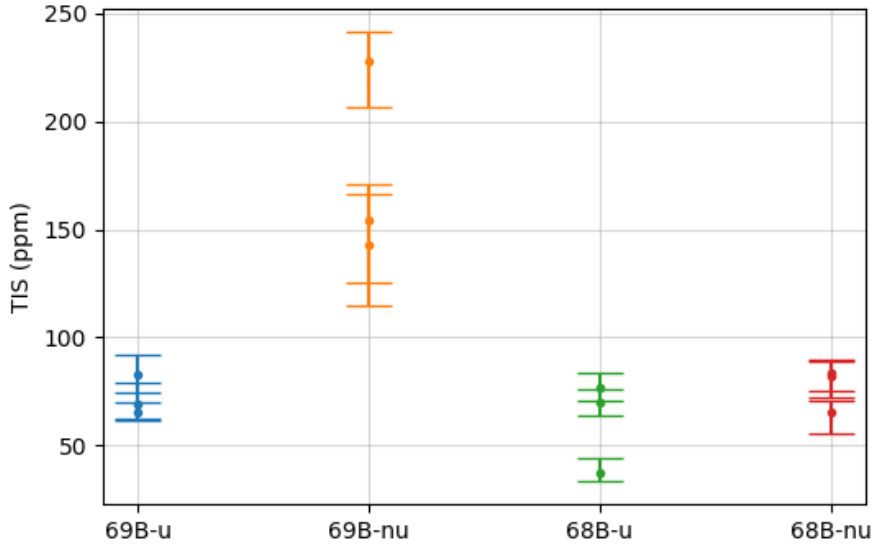

Figure 4.6: TIS estimated from the BSDF measured on different points of 4 baffle samples. Here, "u" refers to "uniform" and "nu" refers to "non-uniform".

To calibrate the setup, a reference line was obtained by making the measurements with the diffusive cap on. This was done once at the start and once at the end of each day, to investigate whether there were any significant changes. The results are shown in Table 4.4. We found that this slope does not change significantly (less than 7%) in a day or between different days.

Date	Slope (10^{-4} A/W)
start of day 22/03/2023	2740 ± 5
end of day 22/03/2023	2761 ± 7
start of day 24/03/2023	2618 ± 9
end of day 24/03/2023	2798 ± 6

Table 4.4: Reference slope measurements.

The value used for the calculations was taken as the average of these values, $(2729 \pm 67)10^{-4}$ A/W.

Eq. 3.13 was used to obtain an estimation of the TIS ignoring corrections for systematic losses in the integrating sphere. The TIS is calculated from the slope m_s of the sample, m_{ref} of the reference and m_∞, which accounts for the air contribution.

To estimate m_∞, we let the sphere open and place a dumper in transmission at

different positions from the sphere. For each position, we measured the corresponding slope of the scattered power against the impinging power. We then made a plot of the slope against the distance (see Fig. 4.7) and, from a fit with Eq. 3.12, we infer m_∞. With this, we find $m_\infty = (26 \pm 2)10^{-6}$ A/W.

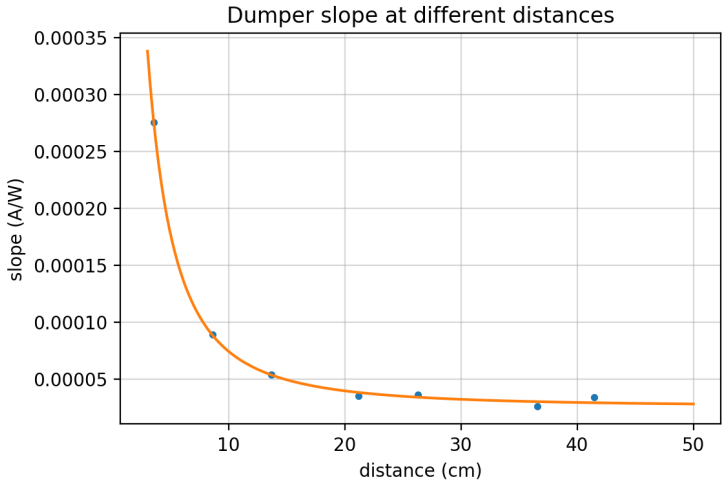

Figure 4.7: Measurement of air contribution on TIS measured with the integrating sphere.

We then measured the samples on multiple positions, sliding them horizontally but at a similar distance from the sphere and finding the slope m_s for each position. The fitted data for each sample is shown in Fig. 4.8. The values of the TIS for each sample are shown in Table 4.5, from which we again noticed that the non-uniform samples seem to have greater variance in the slope and TIS than the uniform ones.

Although the spot where the laser light was impinging was approximately central on the sample, not hitting the stripe of different texture on the non-uniform samples, we considered the possibility that the larger variance on those samples was being caused by an influence of the stripe. We then repeated the measurements with the samples positioned at a lower height, such that the spot where the laser beam was impinging on the sample was far from the stripe. For comparison, Fig. 4.9 reports this new set of measurements (far from the stripe) in blue, together with the previous measurements reported in red. While we still found a similar amount of variability between different points, there does not seem to be a significant difference between the measurements close and far from the stripe. The values of the TIS measured at a lower height for the non-uniform samples are shown in Table 4.6. In Fig. 4.10, all TIS results for each sample are shown.

From Fig. 4.8a, we observe a big spread in the vertical direction for the measurements of sample 69B-Uniform in comparison to the other samples, which indicates a large variability of the power-independent background. This is likely related to the fact that this measurement was the only one made on the first day, together with the measurement of the air contribution, while all other measurements were made on the second day. The variability in the background could be due to the amount of people

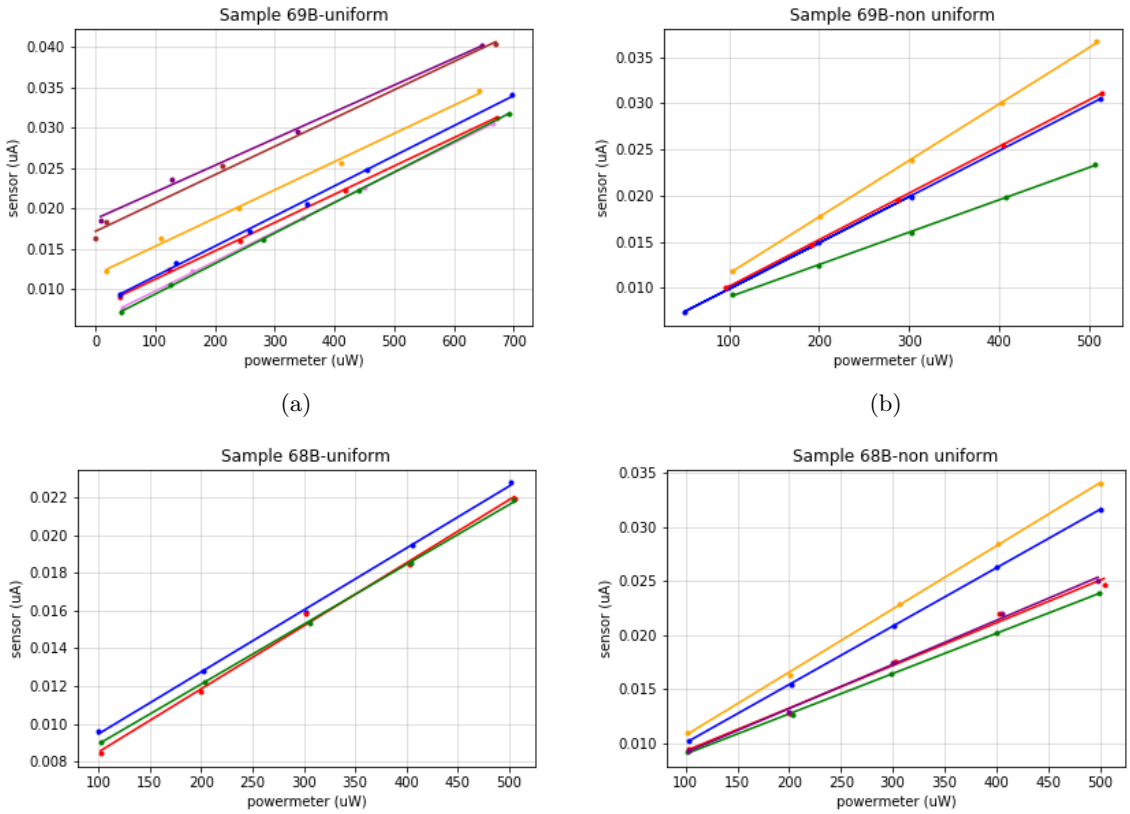

(a) (b)

(c) (d)

Figure 4.8: Measurements performed on all 4 baffle samples with the integrating sphere. The vertical axis contains the current measured by the detector in the sphere and the horizontal axis contains the fraction of the incident power measured with a power meter behind the first mirror in the setup.

Sample	69B Uniform	69B Non-uniform	68B Uniform	68B Non-uniform
Measurements (ppm)	35 ± 9	89 ± 9	26 ± 9	50 ± 10
	43 ± 9	91 ± 9	30 ± 10	103 ± 9
	40 ± 9	130 ± 10	22 ± 9	42 ± 9
	45 ± 9	35 ± 9		120 ± 10
	34 ± 9			60 ± 10
	30 ± 10			
	30 ± 10			
Mean$\pm$ MR	37 ± 8	90 ± 48	26 ± 4	75 ± 78

Table 4.5: Measurements of the TIS performed with the integrating sphere for each baffle sample. The mean TIS measured for each sample is presented with the midrange (MR).

working in the laboratory, which could create shadows from environmental light.

68B Non-uniform, lower height	69B Non-uniform, lower height
40 ± 10	200 ± 10
51 ± 9	56 ± 9
80 ± 10	190 ± 10
130 ± 20	

Table 4.6: Repeated TIS measurements for non-uniform samples (ppm).

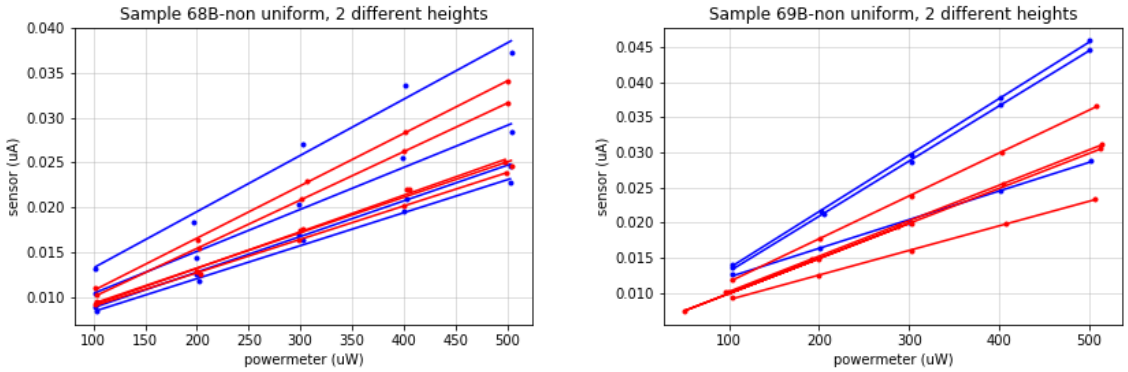

(a) (b)

Figure 4.9: Comparison between measurements taken at different heights on non-uniform samples

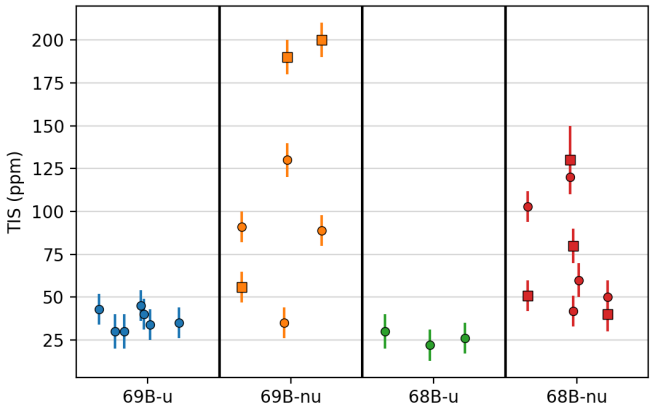

Figure 4.10: Multiple measurements of the TIS with the integrating sphere for each of the samples. Here, "u" refers to uniform, and "nu" refers to non-uniform. The squares represent the measurements made at a lower height while circles represent the other measurements at higher height. The points were purposely plotted at a random offset on the x-axis for better visualization.

The TIS measured directly with the integrating sphere does not account for the losses α and β as described in Section 3.2.1. In order to compare these measurements with the TIS calculated from integrating the BRDF measurements, the latter also needs to be corrected for these losses, which we can do by numerical integration since we have an out-of-plane scattering model fitted to the BRDF data. Since we do not measure the exact same points on the sample with the scatterometer and the integrating sphere, the fit of the averaged BRDF of each sample was used and the corrections were applied to the average value measured with the integrating sphere.

Considering the fact that the samples were not perfectly touching the sphere during measurements, β_s was calculated for a total distance between the sample and the diffusive material in the sphere of 4 mm. From Eq. 3.15, we estimate the final value of the TIS accounting for systematic losses. The values of α_s and β_s for the samples are shown in Table 4.7.

	69B Uniform	69B Non-uniform	68B Uniform	68B Non-uniform
α_s (%)	2.5	5.2	2.2	3.5
β_s (%)	5.1	2.4	5.9	4.7

Table 4.7: α_s and β_s losses calculated for the samples of candidate materials for the baffles in AdVirgo.

Table 4.8 shows the average TIS values (including repeated measurements of non-uniform samples) measured for each sample before and after corrections for systematic losses in the integrating sphere. This is illustrated in Fig. 4.11. As it can be noticed, the correction is generally smaller than the error bar associated with each point either because of measurement uncertainty or variability across the sample.

	69B Uniform	69B Non-uniform	68B Uniform	68B Non-uniform
uncorrected TIS (ppm)	37 ± 8	110 ± 82	26 ± 4	75 ± 45
corrected TIS (ppm)	41 ± 8	120 ± 87	29 ± 4	82 ± 47

Table 4.8: Average TIS measured with the integrating sphere uncorrected for systematic losses compared to corresponding TIS value after corrections for systematic losses.

The resulting average TIS of each sample corrected for the systematic losses in the integrating sphere, the average TIS estimation from the BSDF measured with the scatterometer, and the estimates by EGO (for which no details are known about how the measurement procedures) are reported in Table 4.9 and illustrated in Fig. 4.12. The uncertainties are given by the midrange of all measurements made for the sample.

In general, the values obtained from the scatterometer data are higher (about 30 to 40 ppm) than the ones obtained with the integrating sphere (with the exception of sample "68B non-uniform"). Despite the higher values, the TIS estimation with

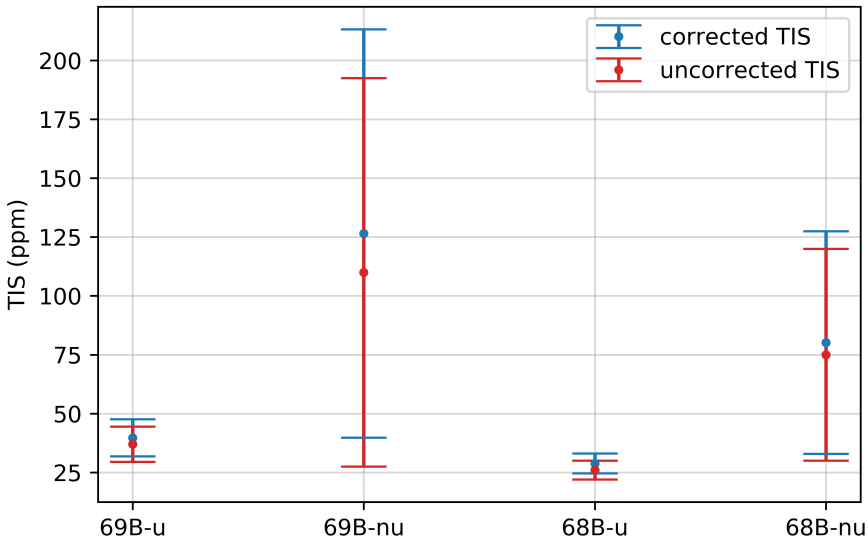

Figure 4.11: Average TIS uncorrected for systematic losses compared to corresponding TIS value after corrections for systematic losses.

the scatterometer seems to follow a similar pattern as the measurements with the integrating sphere and the measurements by EGO.

The increased values could be due to a variety of factors, including some background noise in the scatterometer that is yet to be studied, systematic losses in the integrating sphere that were not accounted for, and an inaccurate BSDF model. As the instruments continue to be developed, the measurement methods and models employed in the estimation of the TIS should be reviewed further for a better understanding of this disagreement and more accurate results.

	69B uniform	69B non-uniform	68B uniform	68B non-uniform
TIS from BSDF (ppm)	73 ± 9	170 ± 42	61 ± 19	77 ± 9
TIS from IS (ppm)	41 ± 8	120 ± 87	29 ± 4	82 ± 47
Measurement by EGO (ppm)	30	210	50	51

Table 4.9: Comparison between TIS estimates by integrating the BSDF measured with the scatterometer, by measuring it directly with the integrating sphere (IS) and the measurement provided by EGO.

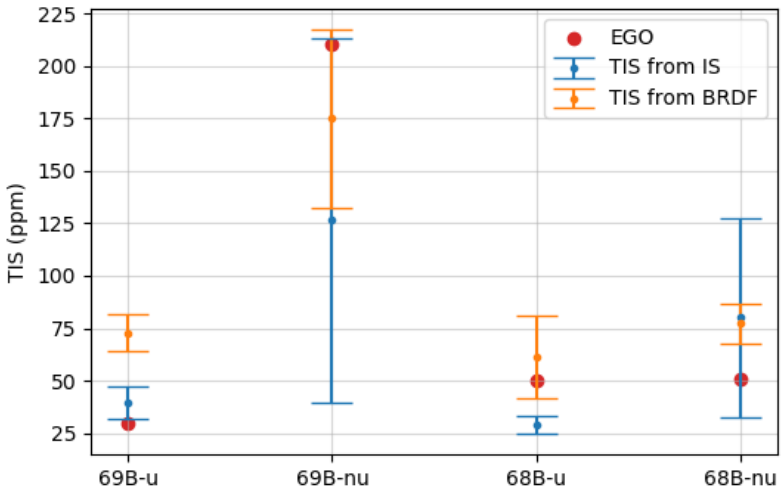

Figure 4.12: Comparison of results with the integrating sphere, with the scatterometer, and with the measurements by EGO. Here, "u" refers to uniform, and "nu" refers to non-uniform.

4.3 Ta2O5 Thin Films

In GW interferometers, the mirrors need to be of very high quality to avoid any source of losses. For this, dielectric coatings are used. They consist of multiple layers with alternating high and low refractive indices, so each boundary between two layers acts as a mirror. The small fraction of light that is transmitted through the first boundary still goes through a series of other layers, being reflected at each boundary. This way, depending on the number of layers, one can set the desired reflectivity of the coated optics. Each layer has a thickness of 1/4 of the laser's wavelength to ensure that every reflection has the same phase, creating constructive interference on the reflected beam.

Thermal noise is generated due to the random motion of the molecules in the mirror or in the coating, causing fluctuations in the mirror surface. According to the fluctuation-dissipation theorem, the intensity of thermal noise increases with the amount of mechanical losses caused by internal friction in the material, as well as with the temperature. The losses in the coating are significantly higher than the losses in the mirror, so many studies have been done to find the best materials to be used for the coatings and techniques that can reduce the thermal noise due to mechanical losses. It has been shown that annealing processes can significantly reduce coating losses [17]. They involve heating the material to a certain temperature for a certain amount of time. This, however, can create crystals in the material that have a different refractive index from the amorphous regions, leading to scattering of light.

Good candidate materials for the low-refractive-index and high-refractive-index layers of the coating are SiO2 and Ta2O5, respectively, due to their low absorption

at 1064 nm [17], the laser wavelength used in advanced detectors. In this section, measurements of samples of SiO2 with a 200 nm coating of Ta2O5 performed with the scatterometer are presented. The samples received rapid thermal annealing treatments at different temperatures. The scatterometer measurements were used to study how the amount of scattering relates to the temperature used in the treatment.

Three samples were measured. They received the thermal treatment for 8 minutes at $723°C$, $744°C$, and $765°C$. We performed the measurements on 3 different positions of each sample, with the minimum angle of incidence allowed by the instrument $\theta_i = 6.5°$, and measured from an angle $\theta_s = 13.5°$ to $163.5°$, avoiding going over the specular reflection and transmission with the detector, in steps of $0.5°$. We also measured a sample "as-deposited" (AD), which received no thermal treatment. The measured BSDFs are shown in Fig. 4.13.

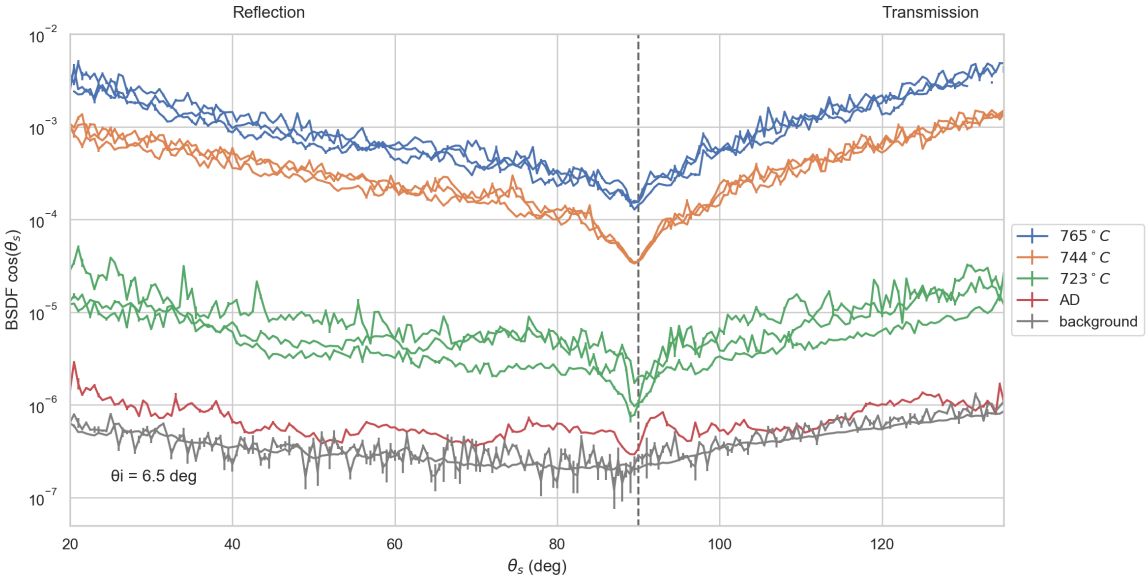

Figure 4.13: BSDF of Ta2O5 thin films measured with the scatterometer. The different samples are indicated by the temperature at which they received the treatment and compared to a sample that received no treatment (AD).

The measurements show a trend in the amount of scattering with the temperature, which is expected due to crystallization at higher temperatures. To study how much this change is, the BRDF was fitted with the GHS model for smooth surfaces in the plane of incidence. For this, the average of the three measurements of the BSDF taken from $\theta_s = 13.5°$ to $\theta_s = 85°$ was used. The resulting fit is shown in Fig. 4.14.

The data seems to have an unexpected increase toward 90°, which has also been observed in the data described in 4.2 but with a much smaller magnitude. The cause for this is still unknown. To understand whether it is being caused by the cosine term when converting the power into BSDF, both the data and the model were multiplied by the cosine of the scattering angle. Fig. 4.15 shows the resulting plot, in which we see that the data remains approximately constant after about 40°, while the BRDF

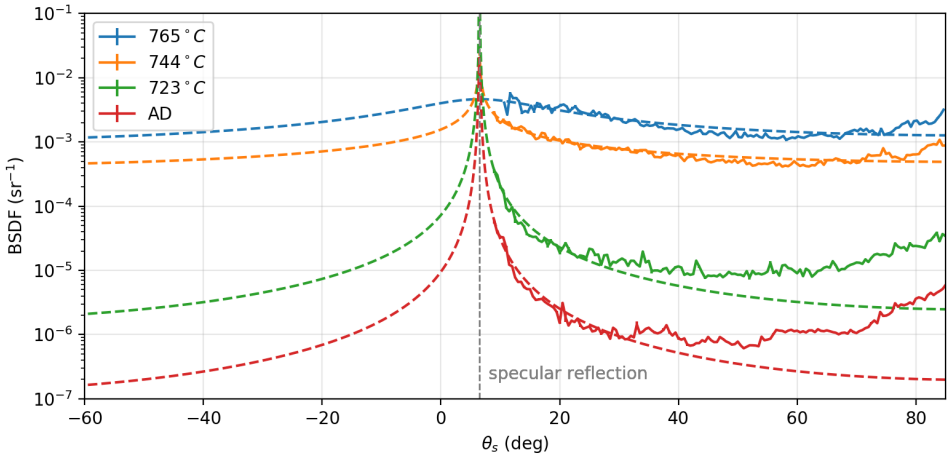

Figure 4.14: Averaged BRDF measured with the scatterometer of SiO2 samples with a 200 nm coating of Ta2O5 that received rapid thermal annealing treatments at different temperatures, fitted with the GHS model (dashed lines).

is expected to decrease at larger angles. The fact that this effect is larger for samples that produce lower scattering suggests that this is being caused by some background contribution, which would also be dependent on the properties of the sample since the value of the BRDF when it becomes constant is different for each sample. In fact, the BSDF of the AD sample is especially close to the background level, meaning it is probably affected at least by the constant background noise.

If the increase toward large angles is a physical effect intrinsic to the surface of the sample, the model is not the best representation of the scatter in this case. If it is being caused by a background contribution, part of the shape of the BRDF is hidden under noise, distorting the fit. Since the fraction of the data affected by this effect is too big for a reliable fit of the unaffected data, the TIS was calculated in two ways: by inserting the parameters from the fit of the entire BRDF data into the GHS model and performing a numerical integration of it, and by performing a numerical integration of the data directly. For the integration using only the data, we do not have the region around the specular reflection or the region at negative θ_s. The integral was then performed by rotating the region where the data is available by 360° around the angle of specular reflection, assuming that the BRDF is radially symmetric. This does not include the region of the peak, however, the contribution of the peak to the TIS has been shown to be small ($\approx 10\%$).

The TIS calculated with the two methods for each sample are presented in Table 4.10 and shown in Fig. 4.16. This is shown with and without the measurement of the AD sample since this is the least reliable measurement due to its proximity to the background noise and to ease visualization. Uncertainties in the fit were calculated with the bootstrap method, taking the 95% confidence interval. The two integration methods give very similar results, with a maximum difference of 13%.

Although the exact value estimated for the TIS is not very reliable due to the

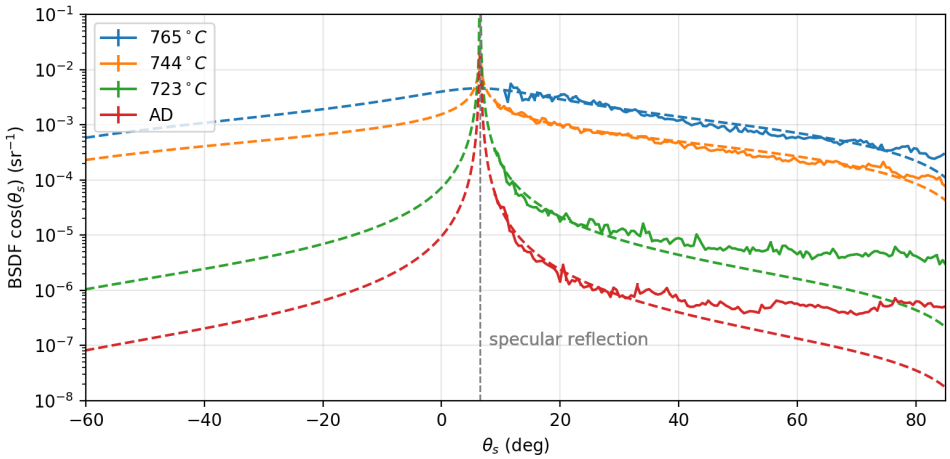

Figure 4.15: Averaged BRDF data and GHS fit (dashed lines) of SiO2 samples multiplied by the cosine of the scattering angle.

Temperature	AD	723 °	744 °	765 °
TIS from data (ppm)	5.3 ± 0.3	47.9 ± 0.3	1784 ± 4	4782 ± 15
TIS from fit (ppm)	4^{+10}_{-3}	34^{+20}_{-13}	1994^{+86}_{-87}	5400^{+390}_{-300}

Table 4.10: TIS calculated by numerically integrating the data and by integrating the fit of the data of SiO2 samples with a Ta2O5 coating, which received thermal treatments at different temperatures.

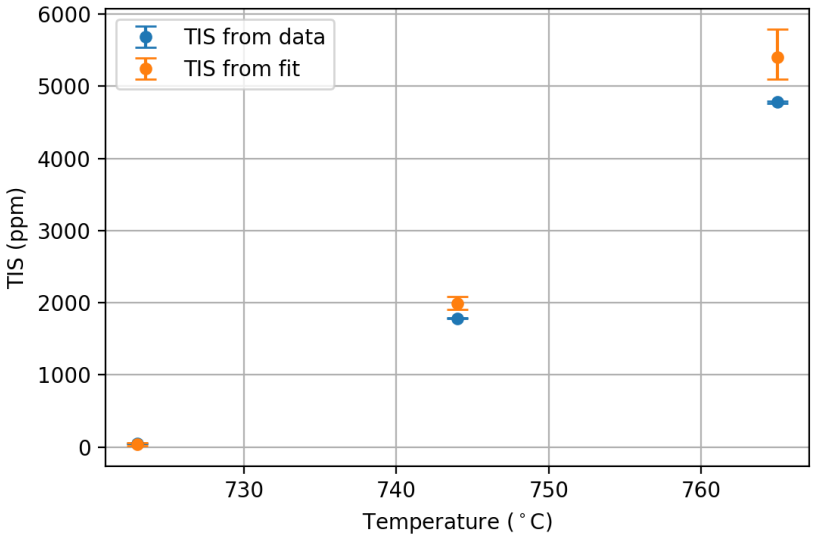

(a) Excluding sample that received no treatment.

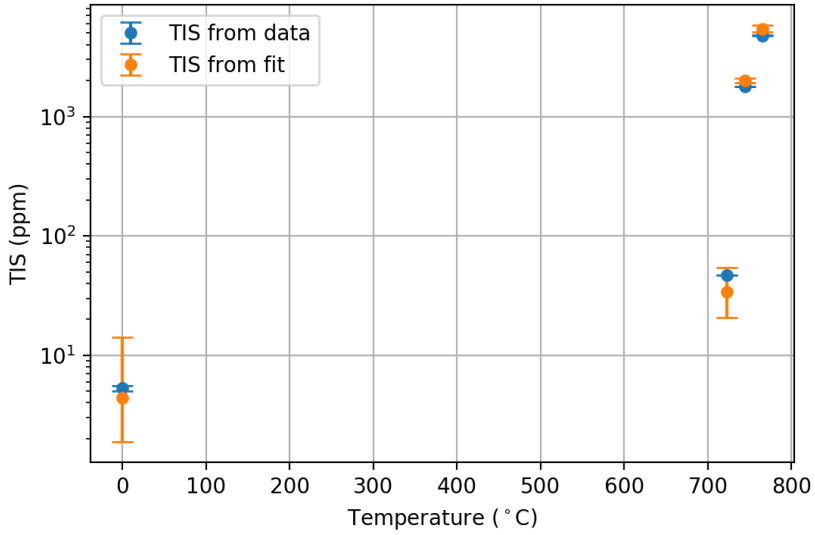

(b) Including sample that received no treatment at 0° C (in log scale for better visualization).

Figure 4.16: TIS calculated for the samples by integrating the fit and by numerically integrating the data.

assumptions on the shape of the BRDF made by both integration methods, the trend with the temperature is clear: it can be seen that the TIS increases with temperature, as expected due to crystallization. Upcoming measurements on similar samples are expected with the integrating sphere for more accurate results. Since there is still an interest in the annealing process to reduce mechanical losses, a compromise must be found. In future studies, the crystal distribution will be studied through X-ray diffraction analysis and optical microscopy to investigate how it is related to the treatment temperature and the amount of scatter in more detail.

5 Conclusion

In this thesis, I have worked to fully characterize, also in terms of losses and systematic effects, two experimental setups to measure scattered light from a sample: a scatterometer, to measure the BSDF, and an integrating sphere, to measure the TIS. The instruments were built with the purpose of characterizing samples representative of candidate materials for current and future gravitational wave detectors to help minimize the issue of stray light. As also part of this work, these two instruments were gathered together and installed in a new facility hosted in a clean room, which allowed us to implement a few upgrades.

One of the upgrades was the addition of an integrating sphere in the same setup. With the use of flip mirrors, it is possible to easily direct the laser light towards either instrument. Three (and a future fourth) lasers were included in the setup, with wavelengths corresponding to the ones used in current advanced detectors and candidate wavelengths for the Einstein Telescope. A telescope was designed for each laser to control the beam spot size on the sample and study how small imperfections on the surface affect the scatter. The new design of the scatterometer allows us to make measurements closer to specular reflection for obtaining more information on the shape of the BSDF. Unlike in the previous setup, the entire instrument and optics are shielded from environmental light by black panels.

The telescopes for changing the beam spot size on the sample were designed based on optical simulations. They all consist of a system of 3 lenses, in which one of them is moved to regulate the spot size. The choice of which lens is movable in the setup was chosen separately for each wavelength, with the goal of achieving a big spot size range without having a telescope that is too sensitive to the lens position. The movable lens was placed on a linear translator and the telescope was characterized for one of the wavelengths, at 1064 nm. With this, we are able to achieve a spot size between $265\mu m$ and $1181\mu m$ on the sample. The telescopes for the other lasers are still to be characterized, but they are expected to reach a similar range.

For making measurements with the integrating sphere, a method was developed to account for the background contribution. This includes making an initial reference measurement and using a dumper at varying distances from the sphere to measure the contribution due to scattering on the air. The latter is a more time-consuming procedure, but it was shown that the air contribution does not tend to fluctuate significantly over time in the clean room, so it does not need to be calculated before every measurement. The value of the TIS with the integrating sphere is calculated based on these two quantities and on the measurement of the sample, which is performed

for multiple values of the incident power.

Systematic losses in the integrating sphere also had to be considered. The openings for the incident beam and specular reflection, as well as the spacing between the sample and the instrument, cause some of the scattered light to be lost. A method to calculate these losses for a certain sample was presented, provided that measurements with the scatterometer are also available. Based on simulations and some preliminary measurements, these losses are estimated to be about 10% in total. This value, however, needs to be estimated again when more measurements are available since the samples used for this were few.

The measurements with the scatterometer are easier to be done since the background noise can be simply subtracted from the measurement. It was also shown that, for most measurements, the background signal is many orders of magnitude lower than the sample measurement, so it can be disregarded. The amount of Rayleigh scattering on air particles in the laboratory was also studied based on simulations, allowing for an estimation of the contribution of this to the BSDF of background signal, found to be in the order of $10^{-8} sr^{-1}$.

We were interested in comparing measurements made with the scatterometer to those made with the integrating sphere. For this, we integrate the BSDF measured with the scatterometer to obtain the TIS, which can be compared to the direct measurement of the TIS with the integrating sphere. Since the scatterometer only measures scattering in the plane of incidence, a model describing the BSDF was needed to fit the data and predict the scattering behavior out-of-plane.

A review of models of the scattering distribution was done and the Generalized Harvey-Shack model was chosen because of its wide applicability. We used the smooth-surface approximation of this model, which has a simple form and applies to all samples of our interest. The comparison between measurements with the scatterometer and the integrating sphere was made for four samples of candidate materials for the baffles at AdVirgo, which showed that the TIS obtained with the two methods is similar, but some disagreement is still present and requires further investigation.

Samples of SiO2 with a Ta2O5 coating were also measured with the scatterometer and the TIS was estimated based on the model. These samples are representatives of anti-reflection layers used on mirrors in the interferometers and were subject to a rapid thermal annealing treatment at different temperatures. A trend was shown in the amount of scatter with the temperature used in the treatment, showing that, although annealing processes can reduce mechanical losses in these materials, it can also increase scattering and generate stray light in the system.

The instrument is currently in its final stages of construction with the upgraded setup. Together with the methods and models presented here, it has been shown to make accurate measurements of the BSDF and the TIS for various samples. With this, it will be possible to relate material properties to the shape and intensity of the scattering distribution, to understand the effect of different particulates on the scatter, and to study how each surface interacts with incident light of different wavelengths, beam radius and polarization. This can later be used for the choice of materials used in future interferometers, reducing the amount of stray light in the system, as well as giving essential information for the estimation of the stray light contribution to the noise floor of these instruments.

References

[1] Acernese, F. et al. "Status of Advanced Virgo". In: *EPJ Web Conf.* 182 (2018), p. 02003. DOI: 10.1051/epjconf/201818202003. URL: https://doi.org/10.1051/epjconf/201818202003.

[2] Javier Alda. "Laser and Gaussian Beam Propagation and Transformation". In: *Encyclopedia of Optical Engineering* (Jan. 2003).

[3] C. Asmail et al. "Rayleigh scattering limits for low-level bidirectional reflectance distribution function measurements". In: *Appl. Opt.* 33.25 (Sept. 1994), pp. 6084–6091. DOI: 10.1364/AO.33.006084. URL: https://opg.optica.org/ao/abstract.cfm?URI=ao-33-25-6084.

[4] Clara Asmail, Albert Parr, and Jack Hsia. "Rayleigh Scattering Limits for Low-Level Bidirectional Reflectance Distribution Function Measurements: Corrigendum". In: *Applied optics* 38 (Nov. 1999), pp. 6027–8. DOI: 10.1364/AO.38.006027.

[5] Diego Bersanetti et al. "Advanced Virgo: Status of the Detector, Latest Results and Future Prospects". In: *Universe* 7.9 (Aug. 2021), p. 322. DOI: 10.3390/universe7090322.

[6] Michael H. Brill. "Seeing the Light: Optics in Nature, Photography, Color, Vision, and Holography, By David S. Falk, Dieter R. Brill, and David G. Stork, Harper and Row, New York, 1986, 446 pp. Price: $35.50". In: *Color Research & Application* 12.3 (1987), pp. 156–157. DOI: https://doi.org/10.1002/col.5080120310. eprint: https://onlinelibrary.wiley.com/doi/pdf/10.1002/col.5080120310. URL: https://onlinelibrary.wiley.com/doi/abs/10.1002/col.5080120310.

[7] Michael Bukshtab. *Photometry, Radiometry, and Measurements of Optical Losses*. eng. 2nd ed. Vol. 209. Springer series in optical sciences, v. 209. Netherlands: Springer Nature, 2019. ISBN: 9811077452.

[8] Samuel D. Butler, Stephen E. Nauyoks, and Michael A. Marciniak. "Comparison of microfacet BRDF model to modified Beckmann-Kirchhoff BRDF model for rough and smooth surfaces". In: *Opt. Express* 23.22 (Nov. 2015), pp. 29100–29112. DOI: 10.1364/OE.23.029100. URL: https://opg.optica.org/oe/abstract.cfm?URI=oe-23-22-29100.

[9] LIGO Caltech. *Why Detect Them?* URL: https://www.ligo.caltech.edu/page/why-detect-gw#:~:text=Detecting%20and%20analyzing%20the%20information,glimpses%20of%20un%2Dseeable%20wonders. (visited on 08/08/2023).

[10] Beatrice D'Angelo. "Numerical Simulations of Stray Light in Virgo". PhD thesis. Genoa U., 2022. DOI: 10.15167/d-angelo-beatrice_phd2022-06-17.

[11] Michael G. Dittman. "K-correlation power spectral density and surface scatter model". In: *Optical Systems Degradation, Contamination, and Stray Light: Effects, Measurements, and Control II*. Ed. by O. Manuel Uy, John C. Fleming, and Michael G. Dittman. Vol. 6291. International Society for Optics and Photonics. SPIE, 2006, 62910R. DOI: 10.1117/12.678320. URL: https://doi.org/10.1117/12.678320.

[12] Aristide C. Dogariu and Glenn D. Boreman. "Autocorrelation Function of Smooth Surfaces from Integrated Wavelet Transforms". In: *Proceedings of SPIE* 2471 (1995).

[13] Eric C. Fest. *Stray Light Analysis and Control*. SPIE—The International Society for Optical Engineering, 2013.

[14] Éanna É Flanagan and Scott A Hughes. "The basics of gravitational wave theory". In: *New Journal of Physics* 7.1 (Sept. 2005), p. 204. DOI: 10.1088/1367-2630/7/1/204. URL: https://dx.doi.org/10.1088/1367-2630/7/1/204.

[15] Francesco Flocco. "Scattered Light Studies for GW Detectors". Internship Report. 2023.

[16] Stefano Gozzo. "Measurement of ultra-low optical absorption in mirror substrates for the next-generation gravitational wave detectors". MA thesis. University of Padua, 2021. URL: https://hdl.handle.net/20.500.12608/21218.

[17] M Granata et al. "Amorphous optical coatings of present gravitational-wave interferometers*". In: *Classical and Quantum Gravity* 37.9 (Apr. 2020), p. 095004. DOI: 10.1088/1361-6382/ab77e9. URL: https://dx.doi.org/10.1088/1361-6382/ab77e9.

[18] James Harvey and Richard Pfisterer. "Comparison of the GHS Smooth and the Rayleigh-Rice surface scatter theories". In: Sept. 2016, p. 996103. DOI: 10.1117/12.2237081.

[19] Hyperphysics. *Blue Sky*. URL: http://hyperphysics.phy-astr.gsu.edu/hbase/atmos/blusky.html.

[20] Andrey Krywonos. "Predicting Surface Scatter Using A Linear Systems Formulation Of Non-paraxial Scalar Diffraction". PhD thesis. University of Central Florida, 2006.

[21] Andrey Krywonos, James Harvey, and Narak Choi. "Linear systems formulation of scattering theory for rough surfaces with arbitrary incident and scattering angles". In: *Journal of the Optical Society of America. A, Optics, image science, and vision* 28 (June 2011), pp. 1121–38. DOI: 10.1364/JOSAA.28.001121.

[22] G. Mie. *Contributions to the optics of turbid media, particularly of colloidal metal solutions*. Contributions to the optics of turbid media, particularly of colloidal metal solutions Transl. into ENGLISH from Ann. Phys. (Leipzig), v. 25, no. 3, 1908 p 377-445. Feb. 1976.

[23] F. E. Nicodemus. "Reflectance Nomenclature and Directional Reflectance and Emissivity". In: *Appl. Opt.* 9.6 (June 1970), pp. 1474–1475. DOI: 10.1364/AO.9.001474. URL: https://opg.optica.org/ao/abstract.cfm?URI=ao-9-6-1474.

[24] Sidney A. Self. "Focusing of spherical Gaussian beams". In: *Appl. Opt.* 22.5 (Mar. 1983), pp. 658–661. DOI: 10.1364/AO.22.000658. URL: https://opg.optica.org/ao/abstract.cfm?URI=ao-22-5-658.

[25] Paul R. Spyak and William L. Wolfe. "Scatter from particulate-contaminated mirrors. part 2: theory and experiment for dust and lambda=0.6328 um". In: *Optical Engineering* 31 (Aug. 1992), pp. 1757–1763. DOI: 10.1117/12.58709.

[26] John C Stover. *Optical scattering : measurement and analysis*. 2nd ed. SPIE monograph PM24. SPIE Optical Engineering Press, 1995. ISBN: 0819419346; 9780819419347; 9780819478443; 081947844X; 9781615837397; 1615837396.

[27] Einstein Telescope. *Introduction*. URL: https://www.et-gw.eu/ (visited on 08/08/2023).

[28] The LIGO Scientific Collaboration et al. "GWTC-3: Compact Binary Coalescences Observed by LIGO and Virgo During the Second Part of the Third Observing Run". In: *arXiv e-prints*, arXiv:2111.03606 (Nov. 2021), arXiv:2111.03606. DOI: 10.48550/arXiv.2111.03606. arXiv: 2111.03606 [gr-qc].

[29] Thorlabs. URL: https://www.thorlabs.com/thorproduct.cfm?partnumber=4P4.

[30] A. Thuring and N. Lastzka. *Jammt - just another mode matching tool*. Version 0.24. URL: https://hadoop.apache.org.

[31] Francesca Ticconi, Luca Pulvirenti, and Nazzareno Pierdicca. "Models for Scattering from Rough Surfaces". In: vol. 10. June 2011. ISBN: 978-953-307-304-0. DOI: 10.5772/19318.

[32] Yonghee Won. "A study of scattering characteristics for micro-scale rough surfaces". PhD thesis. Indiana State University, Jan. 2014.